Three-Dimensional Turbulent Bottom Density Currents
From a High-Order Nonhydrostatic Spectral Element Model

by

Tamay Özgökmen[1], Paul Fischer[2], Jinqiao Duan[3] and Traian Iliescu[4]

1. RSMAS/MPO, University of Miami, Miami, Florida

2. Argonne National Laboratory, Argonne, Illinois

3. Department of Applied Mathematics, Illinois Institute of Technology, Chicago, Illinois

4. Mathematics Department, Virginia Polytechnic Institute and State University, Blacksburg, Virginia

Submitted to:

Journal of Physical Oceanography

November 4, 2003

Abstract

Overflows are bottom gravity currents which supply dense water masses generated in high-latitude and marginal seas into the general circulation. In light of oceanic observations which indicate that mixing of overflows with ambient water masses takes place over small spatial and time scales, and studies with ocean general circulation models, which indicate that the strength of the thermohaline circulation is strongly sensitive to representation of overflows in these models, overflow-induced mixing emerges as one of the prominent oceanic processes.

In this study, nonhydrostatic 3D simulations of bottom gravity currents are carried out, as a continuation of an effort to develop appropriate process models for overflows, that would complement analysis of dedicated observations and large-scale ocean modeling. Nek5000, a parallel high-order spectral element Navier-Stokes solver is used as the basis of the simulations. Numerical experiments are conducted in an idealized setting focusing on the start-up phase of a dense water mass released at the top of a sloping wedge. 3D results are compared to results from 2D experiments and laboratory experiments, based on propagation speed of the density front, growth rate of the characteristic head at the leading edge, turbulent overturning length scales and entrainment parameters.

Results from 3D experiments are found to be in general agreement with those from laboratory tank experiments. In 2D simulations, the propagation speed is approximately 20% slower, the head growth rate is 3 times larger, Thorpe scales are 30-50% larger, and entrainment parameter is upto 2 times higher than those in the 3D experiments. The differences between 2D and 3D simulations are entirely due to internal factors associated with the truncation of the Navier-Stokes equations for 2D approximation. It is concluded that in the absence of external factors that will trigger 3D circulation patterns, such as topographic features and/or rotation, 2D dynamics still represent a reasonable approximation to the general evolution of bottom gravity currents.

1. Introduction

A density current or gravity current is the flow of one fluid within another driven by the gravitational force acting on the density difference between the fluids. Density currents occur in a wide variety of circumstances: in the atmosphere, thunderstorm outflows and sea breeze fronts are gravity currents of cold dense air (Houze, 1993). In rivers, turbidity currents whose density derives from suspended mud and silt can control deposition of sediment, and have geological consequences. Other examples of phenomena induced by similar underlying physics are avalanches and ashe clouds rushing down the mountains after volcanic eruptions (Simpson, 1982).

Oceanic gravity currents are of particular importance, as they are intimately related to the ocean's role in climate dynamics. The thermohaline circulation in the ocean is strongly influenced by dense-water formation that takes place mainly in polar seas by cooling (e.g., Dickson et al., 1990; Borenäs and Lundberg, 1988) and in marginal seas by evaporation (e.g., the Mediterranean Sea, Baringer and Price, 1997a). Such dense water masses are released into the large-scale ocean circulation in the form of overflows, which are bottom gravity currents. For instance, intense evaporation in the Mediterranean Sea produces salty water that sinks to the bottom and flows over the sill in the Strait of Gibraltar (Bryden and Kinder, 1991) and forms a bottom density current that descends along the continental slope. If it did not mix with the Atlantic water, the Mediterranean water would be dense enough to sink to the bottom of the Atlantic Ocean. However, observations show that the Mediterranean salinity tongue spreads across the North Atlantic basin at mid-depths (Lozier et al., 1995), because it is diluted by entrainment of the overlying fresh Atlantic water (e.g., Price et al., 1993). Similar considerations apply to other overflows (e.g., Red Sea: Murray and Johns, 1997; Denmark Strait: Girton et al., 2001; 2002). Studies by Jia (2000), Özgökmen et al. (2001) and Özgökmen and Crisciani (2001) indicate another aspect of overflows that has been only recently appreciated in that it has been put forth that the localized and persistent mixing between the Mediterranean overflow and the North Atlantic Water also plays a role in the dynamics of the overlying upper-ocean currents. A systematic comparison between several realistic ocean circulation models for the North Atlantic circulation demonstrated that the large-scale thermohaline circulation is strongly sensitive to the representation of

overflows in these models (Willebrand et al., 2001). Since our ability to predict the long-term behavior of large-scale ocean circulation (and hence, climate) relies primarily on the accuracy of ocean models, it is important that such models accurately represent the dynamics of dense bottom gravity currents, in particular their mixing with the ambient fluid.

Ocean models of the type used for computation of climate scenarios to the present day have inherent problems in modeling the large-scale effects of overflow plumes mostly because these models are not able to reproduce the product of the mixing processes where they enter into the ocean. Models either dilute the outflow water too strongly (e.g., in geopotential vertical coordinate models), thus destroying outflow signal, or they do not allow enough mixing (e.g., in isopycnal coordinate models), resulting in the "wrong" product waters. An accurate representation of the mixing of overflows with ambient water masses is critical because it determines the properties of intermediate and deep water masses in the ocean. It is generally accepted from laboratory experiments (Simpson, 1969) and observations (e.g., Baringer and Price, 1997b) that mixing between density currents and the ambient fluid takes place primarily via vertical shear instability. Overflows have a small vertical scale, typically $100 - 300 \, m$ (Price and Yang, 1998). The embedded overturns are smaller owing to limitations imposed by stable stratification. An explicit representation of mixing in overflows in numerical models requires not only a small vertical grid scale, but also a horizontal grid scale that is small enough to capture the billows forming near the density interface. Oceanic observations indicate that the typical height-to-length ratio of Kelvin-Helmholtz billows is about 0.1 (e.g., Marmorino, 1987). The typical resolution requirements for explicit resolution of billows are 10-30 m in the vertical direction and 100-300 m in the horizontal direction. As overflows propagate with speeds on the $O(1 \, ms^{-1})$, the time scale for the evolution of billows is on the $O(100 \, s)$. Given the typical spatial resolution of $100 \, km \, (5 - 20 \, km)$ and time steps of $O(hour)$ in climate (large-scale ocean) models, spatial and time scales to resolve overflows are computationally prohibitive at the present time.

In addition to model resolution and vertical coordinate system, another issue is that most ocean models are based on hydrostatic primitive equations. According to the hydrostatic approximation, the primary dynamical balance in the vertical momentum equation is between the pressure gradient and gravitational buoyancy acceleration terms. Therefore,

vertical acceleration terms are omitted, which lead to misrepresentation of vertical mixing processes that are of importance in the dynamics of overflows.

Because of the importance of overflows, there has been significant effort to address these dynamical and modeling issues. Significant progress has been achieved in improving the downslope flow of overflows in geopotential vertical coordinate models (e.g., Beckmann and Döscher, 1997; Winton et al., 1998; Killworth and Edwards, 1999; Nakano and Suginohara, 2002). Also, turbulence closures have been tried in terrain-following models (e.g., Jungclaus and Mellor, 2000) and a mixing parameterization based on laboratory experiments (Turner, 1986) has been implemented in isopycnal models with encouraging results (Hallberg, 2000; Papadakis et al., 2003).

Despite the recent progress, a critical issue that remains to be addressed is the details of mixing and entrainment in bottom density currents. The present level of our systematic understanding of such mixing is derived from laboratory tank experiments (Ellison and Turner, 1959; Simpson, 1969; Britter and Linden, 1980; Simpson, 1982; Turner, 1986; Simpson, 1987; Hallworth et al., 1996; Monaghan et al., 1999; Baines, 2001). However, when configured for the small slopes of observed overflows $[O(1^o)]$, the dense source fluid cannot accelerate enough within the bounds of typical laboratory tanks $[O(1\,m)]$ to produce turbulent behavior. For turbulence to occur, laboratory experiments are configured with slopes greater than 10°. It is also difficult to maintain a complex ambient stratification in these tanks.

Given recent advances in numerical techniques and computer power, numerical modeling provides an alternative avenue to investigate these processes. Nonhydrostatic, high-resolution, two-dimensional (2D) simulations of bottom gravity currents have been conducted by Özgökmen and Chassignet (2002) that capture explicitly the major features of such currents seen in laboratory experiments, such as the presence of a head in the leading edge and Kelvin-Helmholtz vortices in the trailing fluid. Subsequently, this model has been used to simulate the part of the Red Sea outflow in a submarine canyon, which naturally restricts motion in the lateral direction such that the use of a 2D model provides a reasonable approximation to the dynamics. It was shown (Özgökmen et al., 2003) that this model adequately captures the general characteristics of mixing in the Red Sea overflow within the limitations

of a 2D model, such as lack of edge effects or intrusions from channel walls associated with the spanwise structure. The 2D numerical model employed in these studies provides simplicity and computational efficiency. However, by allowing only the spanwise component of vorticity, a 2D model imposes an obvious limitation on the equations of motion, hence potentially on the mixing of bottom gravity currents with ambient fluid. Therefore, the logical next step is to conduct three-dimensional (3D) numerical simulations of bottom gravity currents.

In this study, the primary objective is to determine differences between 2D and 3D simulations of bottom gravity currents. To this end, the experimental setup in Özgökmen and Chassignet (2002) is adopted, in which the initial evolution of a dense water mass released at the top of a sloping wedge at a constant angle is explored. Nek5000, a high-order spectral element Navier-Stokes solver (Fischer, 1996, 1997; Fischer at al., 2000; Tufo et al., 1999; Fischer and Mullen, 2001) is used as the basis for our simulations. First, 2D turbulent simulations are conducted. Then, the domain is extended in the spanwise direction and equivalent 3D simulations are conducted. To the knowledge of the authors, the present numerical simulations are the first to explicitly model 3D shear instability in bottom gravity currents propagating over a sloping topography. The differences between 2D and 3D simulations are quantified by comparing the evolution of characteristic features such as the head of the dense plume, Kelvin-Helmholtz waves, speeds of descent, turbulent overturning length scales and entrainment parameters.

The paper is organized as follows: In section 2, the method is outlined and the numerical model introduced. The experimental setup and parameters are outlined in section 3. Qualitative and quantitative comparisons of 2D and 3D simulations are presented in section 4. Finally, the principal results and future directions are summarized in section 5.

2. Approach

2.1 Model requirements

Bottom density currents have been traditionally investigated using so-called "streamtube" models. These models have been useful in examining the path and bulk properties of the Denmark Strait overflow (e.g., Smith, 1975), Weddell Sea overflow (Killworth, 1977), the

Mediterranean overflow (Baringer and Price, 1997b) and initial studies of the Red Sea over-flow (Bower et al., 2000). Various simplifications are required in these models, such as steady state, motionless ambient fluid, simple topography and mixing parameterization based on laboratory experiments. In recent years, there have been a number of studies employing more complex models. Jungclaus and Backhaus (1994) used a primitive equation, 2D (x, y) shallow water model with reduced gravity approximation in the vertical. They conducted idealized experiments to investigate the effects of bottom friction and topography, and also applied their model to the Denmark Strait overflow. Özsoy et al. (2001) used the same model in the analysis of the overflow from the Bosphorus into the Black Sea, and concluded that the slope and fine-scale features of the bottom topography are crucial elements in de-termining plume behavior. Gawarkiewicz and Chapman (1995) used a 3D hydrostatic model to explore the development of a plume with negative buoyancy. They found that the leading edge of the plume forms eddies in the horizontal plane and concluded that instabilities and eddy fluxes are important mechanisms for the transport of dense waters, in contrast to the quasi-steady behavior implied from streamtube models. This conclusion is also supported by numerical studies by Jiang and Garwood (1995, 1996), who used a different 3D, hy-drostatic, sigma-coordinate model. Jiang and Garwood (1998) concluded that topographic variations induce significant changes in the mixing and entrainment between density currents and ambient fluid. Sigma- and isopycnic-coordinate ocean general circulation models have been used to simulate the Mediterranean overflow (Jungclaus and Mellor, 2000; Papadakis et al., 2003) employing various mixing parameterizations (Mellor and Yamada, 1982, and Hallberg, 2000, respectively). These modeling studies have led to a significant understand-ing of bottom density currents in the ocean. However, none of the above mentioned studies explicitly resolve and capture shear instabilities at the density interface between the gravity current and ambient fluid, which lead to mixing and entrainment. This is partly because of inadequate resolution to capture the scales of such motion and partly because of hydrostatic dynamics.

Following nonhydrostatic, high-resolution 2D simulations of bottom gravity currents in idealized (Özgökmen and Chassignet, 2002) and realistic (Özgökmen et al., 2003) setttings, the logical next step is 3D nonhydrostatic modeling of bottom gravity currents. The nu-

merical model used in previous studies is based on strictly 2D (streamfunction-vorticity) formulation and relatively low-order (finite difference) numerics, whereas the high computational cost of 3D simulations necessitates high-order models to minimize the number of grid points and to obtain good scalability on parallel computers. In this study, a state-of-the-art spectral element model is used, the details of which are described in the following.

2.2 Equations of motion

The momentum and continuity equations subject to the Boussinesq approximation can be written as:

$$\frac{\partial u}{\partial t} + u\frac{\partial u}{\partial x} + v\frac{\partial u}{\partial y} + w\frac{\partial u}{\partial z} = -\frac{1}{\rho_0}\frac{\partial p}{\partial x} + \nu_h\frac{\partial^2 u}{\partial x^2} + \nu_h\frac{\partial^2 u}{\partial y^2} + \nu_v\frac{\partial^2 u}{\partial z^2} \ , \tag{1}$$

$$\frac{\partial v}{\partial t} + u\frac{\partial v}{\partial x} + v\frac{\partial v}{\partial y} + w\frac{\partial v}{\partial z} = -\frac{1}{\rho_0}\frac{\partial p}{\partial y} + \nu_h\frac{\partial^2 v}{\partial x^2} + \nu_h\frac{\partial^2 v}{\partial y^2} + \nu_v\frac{\partial^2 v}{\partial z^2} \ , \tag{2}$$

$$\frac{\partial w}{\partial t} + u\frac{\partial w}{\partial x} + v\frac{\partial w}{\partial y} + w\frac{\partial w}{\partial z} = -\frac{1}{\rho_0}\frac{\partial p}{\partial z} - g\frac{\rho'}{\rho_0} + \nu_h\frac{\partial^2 w}{\partial x^2} + \nu_h\frac{\partial^2 w}{\partial y^2} + \nu_v\frac{\partial^2 w}{\partial z^2} \ , \tag{3}$$

$$\frac{\partial u}{\partial x} + \frac{\partial v}{\partial y} + \frac{\partial w}{\partial z} = 0 \ , \tag{4}$$

where (x, y, z) are three spatial dimensions, t time, (u, v, w) three velocity components, p pressure, $g = 9.81 \, m^2 s^{-1}$ the gravitational acceleration, ν_h and ν_v are viscosities in the horizontal and vertical directions. A linear equation of state is used

$$\rho' = \rho_0 \, \beta \, S \ , \tag{5}$$

where ρ_0 is the background water density, $\beta = 7 \times 10^{-4} \, psu^{-1}$ salinity contraction coefficient, and S salinity deviation from a background value. The equation for salinity transport is

$$\frac{\partial S}{\partial t} + u\frac{\partial S}{\partial x} + v\frac{\partial S}{\partial y} + w\frac{\partial S}{\partial z} = K_h\frac{\partial^2 S}{\partial x^2} + K_h\frac{\partial^2 S}{\partial y^2} + K_v\frac{\partial^2 S}{\partial z^2} \tag{6}$$

where K_h and K_v are diffusivities in the horizontal and vertical directions.

Nondimensionalizing by

$$(x, y, z) = H\left(x^*, y^*, z^*\right), \ (u, v, w) = \frac{\nu_h}{H}\left(u^*, v^*, w^*\right), \ t = \frac{H^2}{\nu_h}t^*, \ p = \frac{\rho_0 \, \nu_h^2}{H^2}p^*, \ S = \Delta S \, S^*, \tag{7}$$

where H is the domain depth and ΔS is the amplitude of the salinity range in the system, and dropping $(*)$, equations of motion in 3D become

$$\frac{\partial u}{\partial t} + u\frac{\partial u}{\partial x} + v\frac{\partial u}{\partial y} + w\frac{\partial u}{\partial z} = -\frac{\partial p}{\partial x} + \frac{\partial^2 u}{\partial x^2} + \frac{\partial^2 u}{\partial y^2} + r\frac{\partial^2 u}{\partial z^2} , \tag{8}$$

$$\frac{\partial v}{\partial t} + u\frac{\partial v}{\partial x} + v\frac{\partial v}{\partial y} + w\frac{\partial v}{\partial z} = -\frac{\partial p}{\partial y} + \frac{\partial^2 v}{\partial x^2} + \frac{\partial^2 v}{\partial y^2} + r\frac{\partial^2 v}{\partial z^2} , \tag{9}$$

$$\frac{\partial w}{\partial t} + u\frac{\partial w}{\partial x} + v\frac{\partial w}{\partial y} + w\frac{\partial w}{\partial z} = -\frac{\partial p}{\partial z} - Ra\, S + \frac{\partial^2 w}{\partial x^2} + \frac{\partial^2 w}{\partial y^2} + r\frac{\partial^2 w}{\partial z^2} , \tag{10}$$

$$\frac{\partial u}{\partial x} + \frac{\partial v}{\partial y} + \frac{\partial w}{\partial z} = 0 , \tag{11}$$

$$\frac{\partial S}{\partial t} + u\frac{\partial S}{\partial x} + v\frac{\partial S}{\partial y} + w\frac{\partial S}{\partial z} = Pr^{-1}\left(\frac{\partial^2 S}{\partial x^2} + \frac{\partial^2 S}{\partial y^2} + r\frac{\partial^2 S}{\partial z^2}\right) , \tag{12}$$

where $Ra = (g\,\beta\,\Delta S\,H^3)/\nu_h^2$ is the Rayleigh number, the ratio of the strengths of buoyancy and viscous forces, $Pr = \nu_h/K_h$ the Prandtl number, the ratio of viscous and saline diffusion, and $r = \nu_h/\nu_v = K_h/K_v$ the ratio of vertical and horizontal diffusivities and viscosities.

In 2D, equations (8)-(12) reduce to

$$\frac{\partial u}{\partial t} + u\frac{\partial u}{\partial x} + w\frac{\partial u}{\partial z} = -\frac{\partial p}{\partial x} + \frac{\partial^2 u}{\partial x^2} + r\frac{\partial^2 u}{\partial z^2} , \tag{13}$$

$$\frac{\partial w}{\partial t} + u\frac{\partial w}{\partial x} + w\frac{\partial w}{\partial z} = -\frac{\partial p}{\partial z} - Ra\, S + \frac{\partial^2 w}{\partial x^2} + r\frac{\partial^2 w}{\partial z^2} , \tag{14}$$

$$\frac{\partial u}{\partial x} + \frac{\partial w}{\partial z} = 0 , \tag{15}$$

$$\frac{\partial S}{\partial t} + u\frac{\partial S}{\partial x} + w\frac{\partial S}{\partial z} = Pr^{-1}\left(\frac{\partial^2 S}{\partial x^2} + r\frac{\partial^2 S}{\partial z^2}\right) . \tag{16}$$

2.3 The numerical model

The small amount of physical dissipation calls for accurate representation of the convective operator such that numerical dissipation and dispersion do not overwhelm physical

effects. Because small-scale structures are transported with minimal physical dissipation, accurate long-time integration is required. These challenges can be efficiently addressed through the use of high-order methods in space and time. The presence of small-scale structures also implies a need for significant spatial resolution in supercritical regions, which may be localized in space.

Spatial discretization of (8)-(12) is based on the spectral element method (SEM) (Maday and Patera, 1989), which is a high-order weighted residual technique based on compatible velocity and pressure spaces that are free of spurious modes. Nek5000 handles general three-dimensional flow configurations, supports a broad range of boundary conditions for hydrodynamics, and accommodates multiple-species transport. Locally, the spectral element mesh is structured, with the solution, data, and geometry expressed as sums of Nth-order Lagrange polynomials on tensor-products of Gauss or Gauss-Lobatto (GL) quadrature points. Globally, the mesh is an unstructured array of K deformed hexahedral elements and can include geometrically nonconforming elements. For problems having smooth solutions, the spectral element method achieves exponential convergence with N, despite having only C^0 continuity (which is advantageous for parallelism). The convection operator exhibits minimal numerical dissipation and dispersion, which is important in the numerical simulation of turbulent flows. The capabilities of the spectral element method have been significantly enhanced through the recent development of a high-order filter that stabilizes the method for convection dominated flows without compromising spectral accuracy (Fischer and Mullen, 2001).

The time advancement is based on second-order semi-implicit operator-splitting methods developed in Perot (1993) and Maday, Patera, and Rønquist (1990). The convective term is expressed as a material derivative, and the resultant form is discretized via a stable backward-difference formula.

Efficient solution of (8)-(12) in complex domains depends on the availability of fast solvers for sparse linear systems. Nek5000 uses as a preconditioner the additive overlapping Schwarz method introduced by Dryja and Widlund (1987) and developed in the spectral element context by Fischer (1997) and Fischer et al. (2000). The key components of our overlapping Schwarz implementation are fast local solvers that exploit the tensor-product form, and a

parallel coarse-grid solver that scales to 1000s of processors (Fischer, 1996; Tufo and Fischer, 1999). The overlapping Schwarz method has provided a significant reduction in work over previous multilevel solvers (Fischer, 1997).

3. Model configuration and parameters

The model domain is configured with a horizontal length of $L_x = 10\,km$. The depth of the water column ranges from $400\,m$ at $x = 0$ to $H = 1000\,m$ at $x = 10\,km$ over a constant slope. Hence the slope angle is $\theta = 3.5°$, which is within the general range of oceanic overflows, such as the Red Sea overflow entering the Tadjura Rift (e.g., Özgökmen et al., 2003). In the 3D case, the domain is extended by $L_y = 2\,km$ in the spanwise direction (Fig. 1a).

The boundary conditions at the bottom are no-slip and no-normal flow for the velocity components, and no-normal flux, $\partial S / \partial \mathbf{n} = 0$ with $\mathbf{n}$ being the normal direction to the boundary, for salinity (Fig. 1a). At the top boundary, free-slip boundary condition is used. The model is entirely driven by the velocity and salinity forcing profiles at the inlet boundary at $x = 0$. The velocity distribution at the inlet (Fig. 1b) matches no-slip at the bottom and free-slip at the top using fourth order polynomials such that the depth integrated mass flux across this boundary is zero. The model is initialized using a salinity distribution of the form

$$S = \frac{1}{2} \exp(-x^{20})[1 - \cos(\pi \frac{1-z}{0.4})] \,,$$

such that the transition from dense water at the bottom to overlying light water is consistent with the flow reversal for the velocity boundary condition (Fig. 1b). Imposing a steady inlet velocity profile independent of the interior dynamics of the density current would lead to either a recirculating flow at the inlet in the case of overestimation or thinning down of the density current as it flows downslope due to inadequate rate of supply. To avoid this, the amplitude of inflow velocity profile was time-dependent and scaled with the propagation speed of the gravity current, which is zero at $t = 0$ and reaches a constant value shortly after release (as shown below). Outflow boundary conditions of the type $\partial \mathbf{u} / \partial x = \partial S / \partial x = 0$ are used at the exit boundary at $x = L_x$. As the interior is initialized with homonegenous, light ($S = 0$) water, the density front propagation is the fastest signal in the system (as opposed to a stratified interior, which may permit faster internal waves). By terminating

the integrations before the nose of density current reaches this boundary, the potential complications involving the outflow boundary are avoided, albeit with the limitation of focusing only on the "start-up" phase of plumes rather than those in a statistically-steady state. Finally, periodic boundary conditions are applied at the lateral boundary for 3D simulations.

The main parameters of the system are the Rayleigh number Ra, the Prandtl number Pr and the diffusivity ratio r. The Prandtl numbers are well known at the microscale ($Pr \approx 7$ for temperature and $Pr \approx 700$ for salinity), but these values are not well defined for larger scales. Here, it is assumed that the impact of turbulent motion is much higher than that of molecular diffusivities on the effective subgrid-scale diffusion, such that there is no difference between turbulent viscosity and diffusivity, and $Pr = 1$. This assumption is supported by laboratory data by Webster (1964). Owing to the high aspect ratio of ocean basins $[O(10^6\,m)$ wide but $O(10^3\,m)$ deep], it is generally assumed that diapycnal diffusivity is very small ($K \approx 10^{-5}\,m^2 s^{-1}$ and $r \ll 1$). This observation clearly applies to large-scale flows as the ocean maintains a characteristic stratification over long time scales. However, this observation no longer applies near boundaries, regions of forcing, localized dissipation and internal waves, all of which characterize overflows. Here, the vertical mixing ratio is chosen such that the horizontal and vertical diffusion terms in the momentum equations are approximately equal, i.e., $r \approx O(H^2/L_x^2) \approx 10^{-2}$, and specifically $r = 2 \times 10^{-2}$ in this study. (When $r \to 1$, the explicit vertical mixing leads to an immediate homogenization of the water column so that the density current does not even flow downslope.) Finally, as Ra represents the range of turbulent scales, the highest Ra permitted by the numerical resolution is used, and $Ra = 5 \times 10^6$ in the experiments presented below. In terms of dimensional quantities, this corresponds to $\Delta S = 1\,psu$ and $\nu_h \approx 1\,m^2 s^{-1}$.

An important factor in the dynamics of oceanic overflows is rotation. The scale at which the Coriolis force becomes comparable to buoyancy force is a complex function of the slope angle, stratification, and friction (e.g., Griffiths, 1986). A simple spatial scale for rotational effects to become important is given by the radius of deformation $\sqrt{g'h}/f$, which is approximately $17\,km$ at midlatitudes with the experimental parameters, as compared to $L_x = 10\,km$. The rotation time scale is $f^{-1} \approx 15000\,s$, while, as shown below, the gravity

currents cross the domain is $\approx 10000\,s$. Hence, the results presented here apply to the phase before impact of rotation starts influencing the flow patterns. Therefore, rotation is neglected here as a first order approximation, and will be the focus of a future investigation. Finally, neglect of rotation allows us to compare results from numerical experiments to those from laboratory experiments, the great majority of which have been conducted in the absence of rotation.

The spectral element method offers a dual approach to convergence: algebraic via elemental grid refinement, and exponential via increase in the order of intra-element interpolation. It is therefore opted to use a minimum number of elements so that (i) the shape of the domain geometry is adequately captured, and (ii) element size is adjusted to better capture the bottom boundary layer. Once the element distribution satisfies these criteria, we increase the spectral truncation degree for the convergence of the technique. In general, the numerical solution of the physical problem of our interest benefits from two well-known features of spectral element models: (i) the lack of numerical dissipation and (ii) excellent phase properties.

The 2D mesh has $K = 400$ elements (50x8 in x, z directions) and the 3D mesh has $K = 4000$ elements (50x8x10 in x, z, y directions). The elements have a smaller vertical scale toward the bottom boundary, and follow topography (Fig. 1b). Therefore, the discretization is free from cronic problems encountered in Cartesian-coordinate models (e.g., Winton et al., 1998). The results presented in this paper are obtained using spectral truncation with a polynomial degree of $N = 10$, which corresponds to 4×10^4 gridpoints for the 2D case, and 4×10^6 gridpoints in the 3D case. Using a time step of $\Delta t = 10^{-6}$ $(0.85\,s)$, the Courant number remains $C < 1$ throughout the simulations. Experiments are repeated also with $N = 5$, and show no significant difference from those with $N = 10$. The model parameters are summarized in Table 1.

The experiments are conducted on a Beowulf Linux cluster consisting of 17 nodes with 1 Gbps ethernet connectivity. Each node has dual Athlon 2 GHz processors with 1024 MB of memory. 2D simulations are conducted on 16 processors and take approximately 2 hours (simulated to real time ratio of ≈ 2), whereas 3D simulations take approximately 9 days on 32 processors (simulated to real time ratio of $\approx 1/60$).

4. Results

The experimental strategy is as follows. The 2D experiment, designated as EXP-2D, is compared to 3D experiments, EXP-3Da and EXP-3Db, which differ only in the spanwise initialization of the density current. We first compare the experiments qualitatively, and then quantitatively using downslope propagation speeds, growth rates of the head, turbulent overturning length scales and entrainment parameters.

4.1 Description of the experiments

The evolution of the salinity distribution in EXP-2D is shown in Fig. 2a. The system is initialized as described in section 3 and starts from rest. The initial development of the system is that of the so-called lock-exchange flow (e.g., Keulegan, 1958; Simpson, 1987), in which the lighter fluid remains on top and the denser overflow propagates downslope. The dense gravity current quickly develops a characteristic "head" at the leading edge of the current (Fig. 2b). The head is half of a dipolar vortex, which is a generic flow pattern that tends to form in two-dimensional systems via the self-organization of the flow (e.g., Flierl et al., 1981; Nielsen and Rasmussen, 1996), and which corresponds to the most probable equilibrium state maximizing entropy (Smith, 1991). Initially, the gravity current is stable, but by the time the current travels half the domain length, the head becomes unstable, exhibiting breaking waves and intense mixing (Fig. 2c). The head grows and is diluted as the gravity current travels down the slope, due to entrainment of fresh ambient fluid. The trailing current, the "tail", displays initially only some patterns of waves, but later (Fig. 2c) the instability near the top of the tail leads to a rolling up of the density interface in lumped vortices separated by a characteristic length scale. This behavior is clearly indicative of the Kelvin-Helmholtz instability, in which waves made up of fluid from the current entrap the ambient fluid (e.g., Corcos and Sherman, 1984). Initially, Kelvin-Helmholtz rolls remain also quite stable, and grow in size by entrainment of ambient fluid and vortex pairing (e.g., Klaassen and Peltier, 1989). Eventually, the system becomes quite complex, exhibiting shedding of dense blobs and localized features resembling hydraulic jumps (Fig. 2d,e). These features were not observed in previous 2D simulations by Özgökmen and Chassignet (2002), which were conducted at lower Ra ($\approx 5 \times 10^4 - 30 \times 10^4$, in our units) because of the numerical

12

dissipation of the 2nd order finite-difference method with respect to that of the spectral-element method. The integration is terminated once the density front reaches $x \approx L_x$ (Fig. 2e).

The 3D experiments are conducted by simply extending the domain in the spanwise direction by $L_y = 2\,km$ and applying periodicity at the lateral boundaries. A sinusiodal perturbation is imposed on the density current initialization in the spanwise direction (Fig. 3a) to accelerate the transition to 3D flow. Other alternatives to facilitate 3D break-down include (i) addition of random perturbations to the equations of motion, or (ii) introduction of y-dependent forcing as velocity or salinity boundary conditions. However, using (i) could potentially degrade the high accuracy of the model numerics, and (ii) could act in a way that it is no longer valid to compare 2D and 3D cases. Here, EXP-3Da simulation remains equivalent to EXP-2D in the spanwise-integrated sense, in terms of parameters, forcing, and initialization.

As the gravity current starts from rest (Fig. 3a), the initial perturbations actually decay such that the current becomes nearly 2D at the beginning (Fig. 3b). As the system gains enough inertia, 3D perturbations amplify (Fig. 3c) and make significant changes in both the head and trailing fluid. The flow along the leading edge of the current is composed of a complex pattern of so-called lobes and clefts, that are highly unsteady (Fig. 3c,d) and well-known features from laboratory experiments tracing back to the work of Simpson (1972). It was conjectured (e.g., Simpson, 1987) that a gravitational rise of the thin layer of light fluid that the gravity current overruns is responsible for the breakdown of the flow at the leading edge. Recently, Härtel et al. (2000) put forth that instability associated with the unstable stratification prevailing at the leading edge between the nose and stagnation point of the front could also account for this behavior. In the trailing fluid, the initial instabilities appear to be 2D Kelvin-Helmholtz rolls that span the entire width of the domain (Fig. 3c). These rolls gradually exhibit transition to 3D (Fig. 3d). The development of spanwise instabilities in Kelvin-Helmholtz rolls has been investigated by Klaassen and Peltier (1991), who classified them into two categories. First are dynamical secondary instabilities that tend to initiate in the vortex core and the interface between strongly rotational and weakly rotational fluid, and develop independently at different growth rates. And second are convective secondary

instabilities in the statically unstable regions which develop as the interface between the two streams overturns. The spanwise variation of shear instability is therefore one of the main mechanisms due to which differences in propagation speed and entrainment can exist between 2D and 3D bottom gravity current simulations.

Several streamwise sections of the salinity distribution are depicted in Fig. 4a for EXP-3Da. While individual sections exhibit coherent features that are similar in size to those obtained in EXP-2D, the spanwise-averaged salinity distribution actually shows less structure (Fig. 4b vs Fig. 2c) because of the variation of shear instabilities in the lateral direction.

EXP-3Db differs from EXP-3Da in that the amplitude of the initial spanwise perturbation is three times larger (Fig. 5a vs Fig. 3a). This experiment is conducted to explore the sensitivity of results to this perturbation. In a qualitative sense, the description of the evolution of the system in EXP-3Db (Fig. 5b-d) follows that of EXP-3Da.

4.2 Speed of descent

It is well-known that in lock-exchange flows (e.g., Keulegan, 1958) and for constant-flux gravity currents (e.g., Ellison and Turner, 1959; Britter and Linden, 1980), the density front quickly reaches a constant speed of propagation. The propagation speed is insensitive to variations in slope angle, since the increase in gravitational force due to greater slope angle is compensated by buoyancy gain due to increased entrainment. In order to conduct a quantitative comparison with previous laboratory and numerical results, the location of density fronts is measured from spanwise-averaged salinity distributions that are sampled every 500 time steps. The position of density fronts X_F as a function of time is shown in Fig. 6 for all experiments. In EXP-2D, the density front propagates at a remarkably constant rate, which is initially followed closely by EXP-3Da,b, but a transition takes place during the time interval $3000\,s \leq t \leq 3500\,s$ in that the 3D experiments start deviating from the 2D case by adopting a faster rate of propagation. This time period coincides with the transition from approximately 2D to 3D instabilities in EXP-3Da,b as shown in Figs. 3,5b,c. As the speed of propagation is closely linked with details of entrainment, Fig. 6 suggests that there is a marked shift in the nature of entrainment following the onset of 3D instabilities.

The relevant scale for the propagation speed is the speed of internal wave associated with

the buoyancy input. In lock-exchange flows, the buoyancy speed scale is $\sqrt{g'h_0}$, where $g' = g\,\beta\,\Delta S \approx 7 \times 10^{-3}\,ms^{-2}$ is the reduced gravity and $h_0 = 200\,m$ is the thickness of dense water at the top of the slope, leading to a speed scale of $1.17\,ms^{-1}$. Even though this scale applies to flows over horizontal surfaces, given the gentle slope in this study, it is reasonable to make comparison to this speed scale. The propagation speed is estimated from $U_F = dX_F/dt$ and the ratio $U_F/\sqrt{g'h_0}$ is plotted in Fig. 7 for all experiments. Following an initial adjustment period, EXP-2D reaches a constant propagation speed ratio of $U_F/\sqrt{g'h_0} \approx 0.73$, whereas EXP-3Da,b oscillate around a mean value of $U_F/\sqrt{g'h_0} \approx 0.85$. The 3D experiments exhibit more variation in U_F probably because of the lobe and cleft instability at the leading edge (Figs. 3,4). Benjamin (1968) estimated theoretically that $U_F/\sqrt{g'h_0} = 1/\sqrt{2}$ when the ratio of dense water depth and total water depth is 0.5 (as near the inlet) and $U_F/\sqrt{g'h_0} = 1$ when the depth ratio is 0.2 (as near the outlet). Fig. 7 indicates that Benjamin's (1968) formulae yield reasonable bounds for the results from numerical experiments. However, note that theoretical results are subject to a variety of assumptions, some of which are clearly unrealistic such as neglect of friction and mixing.

It is therefore of interest to compare the speed of propagation to that from laboratory experiments. Britter and Linden (1980) found, and it also follows from dimensional analysis, that $U_F \sim (g'Q)^{1/3}$ where Q is the volume flux at the inlet. In our experiments, the boundary conditions act in a way to establish quickly a steady volume flux (spanwise-averaged) of $Q \approx 125\,m^2s^{-1}$, and hence yield a propagation speed scale of $0.95\,m\,s^{-1}$. The proportionality constant is estimated from Fig. 8, which shows $U_F/(g'Q)^{1/3} = 0.9$ for EXP-2D, and $U_F/(g'Q)^{1/3} \approx 1.1$ for EXP-3Da,b. These results, in particular those from 3D experiments, are in good agreement with laboratory measurements of Britter and Linden (1980), who found $U_F/(g'Q)^{1/3} = 1.5 \pm 0.2$, and of Monaghan et al. (1999), who reported $U_F/(g'Q)^{1/3} = 1.0 \pm 0.1$.

4.3 Characteristics of the head

The head vortex at the leading edge is a characteristic feature of the start-up phase in bottom gravity currents. The lighter fluid is displaced and lifted up by the leading edge of the gravity current, and strong entrainment takes place into the head from behind (e.g., as

shown in Fig. 11 in Özgökmen and Chassignet, 2002). As the head vortex carries fresh fluid from around the front to the rear of the head, this entrainment leads to the growth of the head. Therefore, it is of interest to quantify the growth rate of the head vortex.

The change in head height $\mathcal{H}$ with downslope distance X is shown in Fig. 9 for all experiments. This figure indicates that the head of the gravity current in EXP-2D grows at approximately constant rate of $d\mathcal{H}/dX \approx 0.051$. The head becomes unstable and breaks down at approximately $X = 7000\,m$, but the remainder of the head continues to grow at the same rate. This rate of growth is in very good agreement with $d\mathcal{H}/dX \approx 0.046$ obtained from the following relationship for $\theta = 3.5°$

$$\frac{d\mathcal{H}}{dX} \approx 13 \times 10^{-3}\,\theta\,, \quad \text{for } 1° \leq \theta \leq 5°\,, \tag{17}$$

that was derived by Özgökmen and Chassignet (2002) based on 2D numerical experiments.

However, Ellison and Turner (1959), Britter and Linden (1980), and Monaghan et al. (1999) obtained from laboratory experiments that

$$\frac{d\mathcal{H}}{dX} \approx 4 \times 10^{-3}\,\theta\,, \tag{18}$$

and the discrepancy between (17) and (18) was surmised to be due to the 2D nature of the simulations by Özgökmen and Chassignet (2002).

As shown in Fig. 9, the growth rate of the head in EXP-3Da,b follows that in EXP-2D until $t \approx 3500\,s$, as all experiments exhibit 2D characteristics during this initial phase. Once the transition to 3D takes place, however, the head growth rate slows down significantly, and a least square fit to data points from EXP-3Da,b yields $d\mathcal{H}/dX \approx 0.015$, which is in very good agreement with $d\mathcal{H}/dX \approx 0.014$ obtained from (18) for $\theta = 3.5°$.

The lengths of head, L, are also estimated from the experiments. Britter and Linden (1980) demonstrate that the growth rates of the length and height of the head are directly proportional, and the aspect ratio of height versus length is a function of the slope angle. Fig. 10 shows that following an initial adjustment period, the ratio $\mathcal{H}/L$ stabilizes around a mean value of

$$\frac{\mathcal{H}}{L} \approx 0.23\,, \tag{19}$$

16

which is in good agreement with the laboratory result of Wood (1965, extracted from Fig. 9 of Britter and Linden, 1980) that $\mathcal{H}/L \approx 0.25$ for gravity current over a slope of $\theta = 5°$.

4.4 Turbulent overturning length scales

While the geometric scales of the head are analysed in section 4.3, it is of interest to quantify all turbulent scales that contribute to mixing. Several relevant length scales in stratified shear flows have been proposed and investigated in detail (e.g., Ozmidov, 1965; Thorpe, 1977; Dillon, 1982; Osborn, 1980; Itsweire et al., 1993; Smyth and Moum, 2000; Tseng and Ferziger, 2001). Some of these length scales require determination of background potential energy, i.e. the minimum potential energy attainable through an adiabatic distribution of the density field (e.g., Winters et al., 1995). This is complicated in the present experimental setup in which boundary fluxes are permitted and a density front propagates over elevation changes. Given that the main objective is to compare turbulent length scales in 2D vs. 3D, we focus on a single scale, the Thorpe scale, which is well-defined, commonly used, and straightforward to compute. Thorpe's (1977) method consists of reordering a model/data density profile, which may contain inversions, into a stable monotonic profile which contains no inversions (e.g., Fig. 11a). Thorpe displacement, d, is the distance that the water parcel must travel vertically in order to reach neutral buoyancy (e.g., Fig 11b). The Thorpe scale, ℓ_T, is defined as the rms of the displacements,

$$\ell_T = < d^2 >_z^{1/2}, \tag{20}$$

which is proportional to the scale of the vertical overturning. It is also useful to define horizontally-averaged Thorpe scale, $\overline{\ell_T}$,

$$\overline{\ell_T} = < \ell_T >_{x,y}, \tag{21}$$

where $<>$ denotes the mean, and the subscripts indicate the direction.

In the numerical experiments, Thorpe scales are calculated in two ways. The first is by selecting a specific location in x and then monitoring spanwise-averaged $\overline{\ell_T}$ as the density front arrives and passes by this location. The second is by calculating $\overline{\ell_T}$ over the entire length of descending plumes. The former reveals the details of coherent structures at specific locations whereas the latter gives an average of all turbulent scales as a function of time.

Fig. 12a shows the average Thorpe scale normalized by the initial dense water depth $(\overline{\ell_T}/h_0)$ near the top of the slope at $x = 1.5\,km$ in all experiments as a function of time. The turbulent scales in both 2D and 3D experiments exhibit pulses of intense overturning separated by periods of laminar flow. This seems to be a manifestation of Kelvin-Helmholtz shear instabilities that tend to occur at this location, as seen in Figs. 2,3,5. $(\overline{\ell_T}/h_0)$ is also calculated near the middle of the slope at $x = 4.0\,km$ (Fig. 12b). The arrival of the large overturning scale associated with the head vortex is followed by smaller scale overturning eddies that seem to be continuous in time rather than episodic as those at $x = 1.5\,km$. Fig. 12 indicates that there is not a significant difference between the scales observed in EXP-3Da and EXP-3Db, whereas those in EXP-2D appear to be somewhat larger. Turbulent scales $(\overline{\ell_T}/h_0)$ averaged over the entire length of descending plumes are shown in Fig. 13a. The growth in the overturning scale in time is only partly due to the growth of the head vortex and is inherently related to the transient nature of the experiments. Fig. 13a confirms that turbulent scales averaged over the entire plume are somewhat larger in 2D than in 3D. The ratio of 2D and 3D scales is quantified in Fig. 13b (after the initial transient), which indicates that on average turbulent scales are 30-50% larger in EXP-2D than those in EXP-3Da,b. This seems to be because, as indicated by Fjortoft's (1953) theorem, 2D turbulence allows for cascade of energy toward both small and large scales, leading to a double cascading spectrum (e.g., Lesieur, 1983). Physically, the inverse energy transfer to large scales results from pairing of Kelvin-Helmholtz vortices, which is well documented in 2D shear flows (e.g., Corcos and Sherman, 1984; Klaassen and Peltier, 1989). In 3D, the energy cascade is toward small scales with the coherent overturning structures being created and maintained under the steady gravitational forcing in the system. Ultimately, the work done by the turbulent overturning eddies determines how much ambient fluid is entrained into the gravity currents, which is quantified in the next section.

4.5 Entrainment

Following the definition of Morton et al. (1956), entrainment is typically quantified as

$$E \equiv \frac{w_E}{U}\,, \tag{22}$$

where w_E is the net entrainment velocity and U is the local current speed. For bottom

gravity currents, this can be approximated as

$$E \approx \frac{\delta h}{\ell} \, , \qquad (23)$$

where δh is the increase (decrease) in the thickness of the dense current due to entrainment (detrainment) over a net streamwise distance of ℓ. Note that while relatively reliable estimates of ℓ or U are possible, w_E or δh can be very difficult to estimate by using profiles from individual sections, in particular for 3D data, due to highly turbulent and time-dependent nature of the flow. Here, we define an entrainment metric, which is similar to previous definitions by Meleshko and van Heijst (1995), Hallworth et al. (1996) and Özgökmen and Chassignet (2002), but has the advantages of being a reliable estimate that applies equally-well to both transient and statistically-steady flows, and being compatible with definitions (22) and (23).

$$E(t) \equiv \frac{V_{total}(t) - V_0(t)}{V(t)} \, , \qquad (24)$$

where V_{total} is the total volume of dense fluid

$$V_{total}(t) \equiv \int_0^{L_y} \int_{x_0}^{X_F(y',t)} h(x',y',t) \, dx' \, dy' \, , \qquad (25)$$

between a reference station of x_0 and the leading edge of the density current X_F. Here, we take $x_0 = 1.5 \, km$ to clear the initial volumes of the dense water in the experiments (e.g., Figs. 2a,3a,5a). The overflow thickness h is calculated from

$$h(x,y,t) \equiv \int_0^{z_0} \eta(x,y,z',t) \, dz' \quad \text{where} \quad \eta(x,y,z,t) = \begin{cases} 0, \text{ when } S(x,y,z,t) < \epsilon \\ 1, \text{ when } S(x,y,z,t) \geq \epsilon \end{cases} \, , \qquad (26)$$

where z_0 is the depth of bottom topography, and $\epsilon = 0.2 \, (psu)$ is the density interface threshold value, which is selected to encompass all contours of salinity shown in Figs. 2-5. In principle, the density interface threshold value can be continuously varied to explore exchanges of fluid between different density layers, however this is beyond the scope of our interest here. V_0 is the input volume of dense fluid at the reference station at the top of the slope (for small θ)

$$V_0(t) \equiv \int_0^t \int_0^{L_y} \int_{z_0+h}^{z_0} u(x_0,y',z',t') \, dz' \, dy' \, dt' \, , \qquad (27)$$

19

and finally

$$V(t) \equiv \overline{\ell}(t)^2 \, L_y \,, \tag{28}$$

where $\overline{\ell}(t) = < X_F(y,t) - x_0 >_y$ is the spanwise-averaged length of the dense overflow measured from the reference station x_0.

Noting that

$$V_{total}(t) = \overline{h}(t) \, \overline{\ell}(t) \, L_y \,, \tag{29}$$

and

$$V_0(t) = \overline{h}_0(t) \, \overline{\ell}(t) \, L_y \,, \tag{30}$$

where $\overline{h}(t)$ and $\overline{h}_0(t)$ are the total (with entrainment) and original (without any entrainment) mean thickness of dense water, (24) can be written as

$$E(t) = \frac{\overline{h}(t) - \overline{h}_0(t)}{\overline{\ell}(t)} \,. \tag{31}$$

It can be seen that (31) is compatible with traditional definitions (22) and (23), but estimation of $\overline{h}(t)$ and $\overline{h}_0(t)$ via volume integrals (25) and (27) leads to reliable estimates of E. (In 2D, integration in y-direction is not necessary, and volume integrals reduce to area integrals.)

Fig. 14 depicts time evolutions of $\overline{h}(t)$ and $\overline{h}_0(t)$ in EXP-2D. Since there is no entrainment initially, $\overline{h_0} \approx \overline{h}$. Once the head starts forming during $1500\,s \leq t \leq 2500\,s$, these quantities start to differ. Note $\overline{h_0}$ stabilizes around a mean value of $150\,m$, whereas $\overline{h}$ shows a steady increase due to entrainment. Similar behavior follows in the other experiments (not shown).

Time evolutions of entrainment parameters $E(t)$ in all experiments are shown in Fig. 15. Entrainment starts at slightly different times because of differences in the initialization of the experiments. The initial entrainment rates are quite comparible because of the 2D nature of the flow during initial stages, as discussed earlier. Entrainment parameter decreases in time in all experiments, because initially entrainment is associated with the growth of the head, which is known to be higher than that in the trailing flow (e.g., Turner, 1986). As the gravity current flows down the slope, the contribution of the head entrainment to overall

20

entrainment decreases. Entrainment in 3D experiments decreases at a faster rate than that in EXP-2D partly because the head starts showing 3D characteristics after $t > 3000\,s$ (Fig. 9) and grows at a smaller rate, as discussed in section 4.3. Generally speaking, it is not surprizing that the entrainment during the start-up phase is higher than that in a phase approaching equilibrium (e.g., Beckmann, 1998). By the end of the integrations, E in EXP-2D is approximately twice as much as those from EXP-3Da,b, which is consistent with the results found about differences in turbulent length scales in section 4.4. For reference, the estimate $E = (5 + \theta) \times 10^{-3}$ given by Turner (1986) based on laboratory experiments of Ellison and Turner (1959) is plotted in Fig. 15 as well. Note, however, that the actual laboratory experiments were conducted for $\theta > 10°$ and the above relationship is extended to $\theta = 3.5°$ in this study. The entrainment parameter in 3D experiments is $E \approx 5 \times 10^{-3}$ at the end of the integrations, but possibly still decreasing. This is somewhat higher than the entrainment parameters observed in oceanic overflows, which are estimated to be in the range of $0.2 \times 10^{-3} \le E \le 2 \times 10^{-3}$ (Baringer and Price, 1997b; based on Mediterranean Sea overflow observations; Özgökmen et al. 2003, based on Red Sea overflow observations and numerical modeling). However, the high entrainment in the numerical experiments could be due to a variety of factors ranging from the time-dependent nature of the flow, differences in slope angles, the neglect of rotation and ambient stratification, and generally, the idealized nature of this investigation.

5. Summary and conclusions

This study is motivated by the fact that most deep and intermediate water masses are released into the large-scale ocean circulation from high-latitude and marginal seas in the form of overflows. In light of observations which revealed that the mixing of overflows with the ambient fluid takes place over very small spatial and time scales (Price et al., 1993; Baringer and Price, 1997a,b; Price and Yang, 1998), and studies with ocean general circulation models that demonstrated that the strength of the thermohaline circulation is very sensitive to details of the representation of overflows in these models (e.g., Willebrand et al., 2001), overflow-induced entrainment is being generally recognized as one of the prominent oceanic processes. The importance of overflows has led to significant effort to improve their

representation in ocean models, and significant progress has been achieved recently (e.g., Beckmann and Döscher, 1997; Winton et al., 1998; Killworth and Edwards, 1999; Jungclaus and Mellor, 2000; Hallberg, 2000; Nakano and Suginohara, 2002; Papadakis et al., 2003).

An important avenue that will complement dedicated observational programs such as those in the Meditteranean Sea (Price et al. 1993), the Red Sea (Bower et al., 2002; Johns et al., 2003, Peters et al., 2003) and the Denmark Strait (Girton et al., 2001) in order to improve parametrizations of overflow processes, is process modeling. However, because of the small space and time scales, fully realistic modeling of overflow processes demands high-resolution, nonhydrostatic models. In recent nonhydrostatic simulations of bottom gravity currents in idealized (Özgökmen and Chassignet, 2002) and realistic (Özgökmen et al., 2003) settings, a 2D model was used, which offers great simplicity and computational efficiency, albeit at the expense of allowing only the spanwise component of vorticity and thus potentially modifying the ways in which mixing and entrainment can take place in a real fluid. Therefore, a logical next step is to conduct 3D numerical experiments. Our primary objective in this study is to explore differences between 2D and 3D nonhydrostatic simulations bottom gravity currents.

3D nonhydrostatic experiments require the use of a sophisticated numerical model that has good convergence characteristics to minimize the number of grid points and time steps, and good scalability on parallel computers. Spectral element models provide characteristics such as minimal numerical dissipation and excellent scalability. Spectral element design combines the geometric flexibility of finite element models with the numerical accuracy of spectral decomposition. It also offers a dual approach to convergence; algebraic via elemental grid refinement and exponential via the increase in the order of intra-element interpolation. The use of the spectral element method for ocean general circulation (hydrostatic) simulations has been pioneered by Iskandarani et al. (1995; 2002; 2003). Here we use Nek5000, a high-order state-of-the-art spectral element Navier-Stokes solver (documented in detail by Fischer, 1996; 1997; Fischer at al., 2000; Tufo and Fischer, 1999; Fischer and Mullen, 2001) as the basis for our simulations. The parallel scaling of Nek5000 on 8168-processor ASCI-Red for a 3D flow simulation was recognized with the Gordon Bell Prize in 1999.

The initial evolution of a dense water mass released at the top of a sloping wedge at a constant angle is explored. Results from a 2D turbulent simulation, denoted EXP-2D, are

compared to those from equivalent 3D simulations, denoted EXP-3Da,b, which are conducted by extending the domain in the spanwise direction. The 3D experiments differ only in the magnitude of the initial spanwise perturbation that is used to facilitate 3D break down. No significant difference is found between the results from the two 3D experiments, but they provide two different realizations, thus increasing the reliability of the results. To the knowledge of the authors, the present numerical simulations are the first to capture explicitly 3D shear instability in bottom gravity currents propagating over a sloping topography.

Qualitatively, evolutions of bottom gravity currents in 2D and 3D are similar, both exhibiting a large vortex in the leading edge and shear instabilities in the trailing fluid. In 3D experiments, both the head vortex and Kelvin-Helmholtz rolls show 2D characteristics spanning the entire width of the domain, but then transition to 3D by exhibiting a break-down of spanwise rolls and the so-called lobe and cleft instability in the leading edge, which is caused by the instability associated with the nose propagation (Härtel et al., 2000) and a well-known feature from laboratory experiments (e.g., Simpson, 1972).

Quantitatively, the propagation speed of the density front is $U_F/(g'Q)^{1/3} \approx 0.9$ (or $U_F = 0.85\,ms^{-1}$) in EXP-2D and $U_F/(g'Q)^{1/3} \approx 1.1$ (or $U_F = 1.0\,ms^{-1}$) in EXP-3Da,b, which are in good general agreement with laboratory results of $(1 \pm 0.1) \leq U_F/(g'Q)^{1/3} \leq (1.5 \pm 0.2)$ (Britter and Linden, 1980; Monaghan et al. 1999) and analytical estimates of Benjamin (1968). The growth rate of the head is $d\mathcal{H}/dX \approx 0.051$ in EXP-2D, in good agreement with the relationship $d\mathcal{H}/dX \approx 13 \times 10^{-3}\theta \approx 0.046$ derived by Özgökmen and Chassignet (2002) based on 2D simulations. However, $d\mathcal{H}/dX \approx 0.015$ in EXP-3Da,b, in very good agreement with $d\mathcal{H}/dX \approx 4 \times 10^{-3}\theta \approx 0.014$ based on laboratory experiments by Ellison and Turner (1959), Britter and Linden (1980) and Monaghan et al. (1999). Hence, the head growth rate is 3 times larger in 2D than in 3D. In order to explore differences in turbulent length scales, Thorpe scales are calculated, which are found to be $30 - 50\%$ larger in 2D than those in 3D. The difference is scales results from cascade of energy to large scales in 2D turbulence.

Differences in the speed of propagation, head growth rates and turbulent length scales clearly point towards differences in the entrainment characteristics in 2D and 3D. A new method for a reliable estimation of entrainment parameter E is introduced, which applies equally well to transient and statistically-steady flows, is compatible with traditional defini-

tions of entrainment, and suitable for processing large data sets in 2D or 3D. It is shown that E in EXP-2D can be 2 times as large as that in EXP-3Da,b. In absolute terms, $E \approx 5 \times 10^{-3}$ in EXP-3Da,b, which compares reasonably well with $E \approx 8.5 \times 10^{-3}$ based on a relationship given by Turner (1986), when extended to the slope angle of this study. The entrainment parameter in the numerical experiments is somewhat higher than those observed in oceanic overflows, which are typically in the range of $0.2 \times 10^{-3} \leq E \leq 2 \times 10^{-3}$. This discrepancy could be explained by a variety of factors ranging from the time-dependent nature of the flow, differences in slope angles, the neglect of rotation and ambient stratification, and generally, the idealized nature of this investigation.

In conclusion, while some differences between 2D and 3D simulations, which arise entirely due to internal factors associated with the truncation of the Navier-Stokes equations for 2D approximation, can be significant in a quantitative sense, 2D results are qualitatively still quite close to those from 3D simulations. Therefore, in the absence of external factors that can trigger 3D circulation patterns, such as topographic variations in the spanwise direction and rotation, 2D approximation provides a computationally inexpensive approach to investigate the general behavior of bottom gravity currents. We surmise that far more significant differences between 2D and 3D results would arise in cases in which topographic slope varies in the spanwise direction, and/or rotational effects are important. These topics will be investigated in the near future.

References

Baines, P.G., 2001: Mixing in flows down gentle slopes into stratified environments. *J. Fluid Mech.*, **443**, 237-270.

Baringer, M. O., and J. F. Price, 1997a: Mixing and spreading of the Mediterranean outflow. *J. Phys. Oceanogr.*, **27**, 1654-1677.

Baringer, M. O., and J. F. Price, 1997b: Momentum and energy balance of the Mediterranean outflow. *J. Phys. Oceanogr.*, **27**, 1678-1692.

Beckmann, A., 1998: The representation of bottom boundary layer processes in numerical ocean circulation models. In *Ocean Modelling and Parameterization*, eds: E.P. Chassignet and J. Verron, pp. 135-154.

Beckmann, A., and R. Döscher, 1997: A method for improved representation of dense water spreading over topography in geopotential-coordinate models. *J. Phys. Oceanogr.*, **27**, 581-591.

Benjamin, T.B., 1968: Gravity currents and related phenomena. *J. Fluid Mech.*, **31**, 209-248.

Borenäs, K.M., and P.A. Lundberg, 1988: On the deep-water flow through the Faroe Bank Channel. *J. Geophys. Res.*, **93**, 1281-1292.

Bower, A.S., H.D. Hunt, and J.F. Price, 2000: Character and dynamics of the Red Sea and Persian Gulf outflows. *J. Geophys. Res.*, **105**, 6387-6414.

Bower, A.S., D.M. Fratantoni, W.E. Johns, and H. Peters, 2002: Gulf of Aden eddies and their impact on Red Sea Water. *Geophys. Res. Lett.*, **29**, doi: 10.1029/2002GL015342.

Britter, R.E., and J.E. Simpson, 1978: Experiments on the dynamics of a gravity current head. *J. Fluid Mech.*, **88**, 223-240.

Britter, R.E., and J.E. Simpson, 1981: A note on the structure of the head of an intrusive gravity current. *J. Fluid Mech.*, **112**, 459-466.

Britter, R.E., and P.F. Linden, 1980: The motion of the front of a gravity current traveling down an incline. *J. Fluid Mech.*, **99**, 531-543.

Bryden, H. L., and T. H. Kinder, 1991: Steady two-layer exchange through the Strait of Gibraltar. *Deep-Sea Res.*, **38** Suppl., S445-S463.

Corcos, G.M., and F.S. Sherman, 1984: The mixing layer: deterministic models of a turbulent flow. Part 1. Introduction and the two-dimensional flow. *J. Fluid Mech.*, **139**, 29-65.

Dickson, R.R., E.M. Gmitrowics, and A.J. Watson, 1990: Deep water renewal in the northern North Atlantic. *Nature*, **344**, 848-850.

Dillon, T.M., 1982: Vertical overturns: a comparison of Thorpe and Ozmidov length scales. *J. Geophys. Res.*, **87(C12)**, 9601-9613.

Dryja, M., and O. B. Widlund, 1987: An additive variant of the Schwarz alternating method for the case of many subregions. Technical Report 339, Dept. of Computer Science, Courant Institute.

Ellison, T.H., and J.S. Turner, 1959: Turbulent entrainment in stratified flows. *J. Fluid Mech.*, **6**, 423-448.

Fernando, H. J. S., 1991: Turbulent mixing in stratified fluids. *Annu. Rev. Fluid Mech.*, **23**, 455-493.

Fischer, P.F. and J. S. Mullen, 2001: Filter-Based Stabilization of Spectral Element Methods. *Comptes rendus de l'Académie des sciences Paris, t. 332, -Série I - Analyse numérique*, 265-270.

Fischer, P.F., 1996: Parallel multi-level solvers for spectral element methods. in *Proceedings of Intl. Conf. on Spectral and High-Order Methods '95, Houston, TX*, A.V. Ilin and L.R. Scott, Eds.

Fischer, P.F., 1997: An Overlapping Schwarz Method for Spectral Element Solution of the Incompressible Navier-Stokes Equations. *J. of Comp. Phys.* **133**, 84–101.

Fischer, P.F., 1998: Projection techniques for iterative solution of $A\underline{x} = \underline{b}$ with successive right-hand sides. *Comp. Meth. in Appl. Mech.*, **163**, 193–204.

Fischer, P.F., N. I. Miller, and H. M. Tufo, 2000: An Overlapping Schwarz Method for Spectral Element Simulation of Three-Dimensional Incompressible Flows. in *Parallel Solution of Partial Differential Equations*. Springer-Verlag, ed. by P. Björstad and M. Luskin, 159-181.

Fjortoft, R., 1953: On the changes in the spectral distribution of kinetic energy for two-dimensional non-divergent flow. *Tellus*, **5**, 225-230.

Flierl, G.R., M.E. Stern, and J.A. Whitehead, 1981: The physical significance of modons: laboratory experiments and general integral constraints. *Dyn. Atmos. Oceans*, **7**, 233-263.

Gawarkiewicz, G., and D.C. Chapman, 1995: A numerical study of dense water formation and transport on a shallow, sloping continental shelf. *J. Geophys. Res.*, **100**, 4489-4507.

Girton, J.B., T.B. Sanford, and R.H. Käse, 2001: Synoptic sections of the Denmark Strait overflow. *Geophys. Res. Lett.*, **28**, 1619-1622.

Griffiths, R.W., 1986: Gravity currents in rotating systems. *Annu. Rev. Fluid Mech.*, **18**, 59-89.

Hallberg, R., 2000: Time integration of diapycnal diffusion and Richardson number dependent mixing in isopycnal coordinate ocean models. *Mon. Wea. Rev.*, **128**(5), 1402-1419.

Hallworth, M.A., H.E. Huppert, J.C. Phillips and S.J. Sparks, 1996: Entrainment into two-dimensional and axisymmetric turbulent gravity currents. *J. Fluid Mech.*, **308**, 289-311.

Härtel, C., E. Meiburg, and F. Necker, 2000: Analisys and direct numerical simulation of the flow at a gravity-current head. Part 1. Flow topology and front speed for slip and no-slip boundaries. *J. Fluid Mech.*, **418**, 189-212.

Houze, R.A., 1993: *Cloud dynamics.* Academic Press, 573 pp.

Iskandarani, M., Haidvogel D.B. and Levin, J.C., 2003: A three-dimensional spectral element model for the solution of the hydrostatic primitive equations. *J. Comp. Physics*, **186/2**, 397-425.

Iskandarani, M., Haidvogel D.B., Levin, J.C., Curchitser E., and Edwards C.A., 2002: Multiscale geophysical modeling using the spectral element method. *Comp. Sci. Eng.*, **4/5**, 42-48.

Iskandarani, M., Haidvogel D.B., and Boyd, J.P., 1995: A staggered spectral element model with application to the oceanic shallow-water equations. *Int. J. Numer. Meth. Fl.*, **20/5**, 393-414.

Itsweire, E.C., J.R. Koseff, D.A. Briggs, and J.H. Ferziger, 1993: Turbulence in stratified shear flows: implications for interpreting shear-induced mixing in the ocean. *J. Phys. Oceanogr.*, **23**, 1508-1522.

Jia, Y., 2000: On the formation of an Azores Current due to Mediterranean overflow in a modelling study of the North Atlantic. *J. Phys. Oceanogr.*, **30**, 2342-2358.

Jiang, L., and R.W. Garwood Jr., 1995: A numerical study of three-dimensional dense bottom plumes on a Southern Ocean continental slope. *J. Geophys. Res.*, **100**, 18,471-18,488.

Jiang, L., and R.W. Garwood Jr., 1996: Three-dimensional simulations of overflows on continental slopes. *J. Phys. Oceanogr.*, **100**, 1214-1233.

Jiang, L., and R.W. Garwood Jr., 1998: Effects of topographic steering and ambient stratification on overflows on continental slopes: a model study. *J. Geophys. Res.*, **103**, 5459-5476.

Johns, W., H. Peters, A.S. Bower, and D.M. Fratantoni, 2002: Red Sea Outflow Experiment (REDSOX): New observations of the descent and spreading of the Red Sea water. *AGU Ocean Sciences meeting*, QS1Q-02, Honolulu.

Jungclaus, J.H., and J.O. Backhaus, 1994: Application of a transient reduced gravity plume model to the Denmark Strait Overflow. *J. Geophys. Res.*, **99**, 12,375-12,396.

Jungclaus, J.H., and G. Mellor, 2000: A three-dimensional model study of the Mediterranean outflow. *J. Mar. Sys.*, **24**, 41-66.

Keulegan, G. H., 1958: The motion of saline fronts in still water. *U.S. Nat. Bur. Stand.*, Report no. 5831.

Killworth, P.D., and N.R. Edwards, 1999: A turbulent bottom boundary layer code for use in numerical ocean models. *J. Phys. Oceanogr.*, **29**, 1221-1238.

Killworth, P.D., 1977: Mixing on the Weddell Sea continental slope. *Deep-Sea Res.*, **24**, 427-448.

Klaassen, G.P. and W.R. Peltier, 1991: The influence of stratification on secondary instability in free shear layers. *J. Fluid Mech.*, **227**, 71-106.

Klaassen, G.P. and W.R. Peltier, 1989: The role of transverse secondary instabilities in the evolution of free shear layers. *J. Fluid Mech.*, **202**, 367-402.

Lesieur, M., 1983: Introduction to two-dimensional turbulence. In *Two-dimensional turbulence, J. Mec. Th. Appl. Suppl.*, R. Moreau ed., pp. 5-20.

Lozier, M. S., W. B. Owens, and R. G. Curry, 1995: The climatology of the North Atlantic. *Prog. Oceanogr.*, **36**, 1-44.

Maday, Y. and A. T. Patera, 1989: Spectral Element Methods for the Navier-Stokes Equations, in *State of the Art Surveys in Computational Mechanics*, ASME, New York, ed. by A. K. Noor, 71-143.

Maday, Y., A. T. Patera, and E. M. Rønquist, 1990: An operator-integration-factor splitting method for time-dependent problems: application to incompressible fluid flow. *J. Sci. Comput.*, **5**(4), 310-37.

Marmorino, G. O., 1987: Observations of small-scale mixing processes in the seasonal thermocline. Part 2 - Wave breaking. *J. Phys. Oceanogr.*, **17**, 1348-1355.

Mellor, G.L. and T. Yamada, 1982: Development of a turbulence closure model for geophysical fluid problems, *Rev. Geophys. Space Phys.*, **20**,851-875.

Meleshko, V. V., and G. J. F. Van Heijst, 1995: Interacting two-dimensional vortex structures: point vortices, contour kinematics and stirring properties. In *Chaos Applied to Fluid Mixing*, eds: H. Aref and M. S. El Naschie, pp. 233-266, Pergamon.

Monaghan, J.J., R.A.F. Cas, A.M. Kos, and M. Hallworth, 1999: Gravity currents descending a ramp in a stratified tank. *J. Fluid Mech.*, **379**, 39-70.

Morton, B.R., G.I. Taylor, and J.S. Turner, 1956: Turbulent gravitational convection from maintained and instantaneous sources. *Proc. R. Soc. Lond.*, **A 234**, 1-23.

Murray, S.P., and W.E. Johns, 1997: Direct observations of seasonal exchange through the Bab el Mandab Strait. *Geophys. Res. Lett.*, **24**(21), 2557-2560.

Nakano, H. and N. Suginohara, 2002: Effects of bottom boundary layer parameterization on reproducing deep and bottom waters in a world ocean model. *J. Phys. Oceanogr.*, **32**, 1209-1227.

Nielsen, A.H., and J.J. Rasmussen, 1996: Formation and temporal evolution of the Lamb-dipole. *Phys. Fluids*, **9**, 982-991.

Osborn, T.R., 1980: Estimates of the local rate of vertical diffusion from dissipation measurements. *J. Phys. Oceanogr.*, **10**, 83-89.

Ozmidov, R.V., 1965: On the turbulent exchange in a stably stratified ocean. *Ivz. Acad. Sci. USSR, Atmos. Oceanic Phys.*, **1**, 853-860.

Özgökmen, T.M., W. Johns, H. Peters, and S. Matt, 2003: Turbulent mixing in the Red Sea outflow plume from a high-resolution nonhydrostatic model. *J. Phys. Oceanogr.*, **33/8**, 1846-1869.

Özgökmen, T. M., and E. Chassignet, 2002: Dynamics of two-dimensional turbulent bottom gravity currents. *J. Phys. Oceanogr.*, **32**, 1460-1478.

Özgökmen, T.M., and F. Crisciani, 2001: On the dynamics of β-plumes. *J. Phys. Oceanogr.*, **31**, 3569-3580.

Özgökmen, T. M., E. P. Chassignet, and C. G. H. Rooth, 2001: On the connection between the Mediterranean outflow and the Azores Current. *J. Phys. Oceanogr*, **31/2**, 461-480.

Özsoy, E., D.D. Iorio, M.C. Gregg, and J.O. Backhaus, 2001: Mixing in the Bosphorus Strait and the Black Sea continental shelf: observations and a model of the dense outflow. *J. Mar. Sys.*, **31**, 99-135.

Papadakis, M.P., E.P. Chassignet, and R.W. Hallberg, 2003: Numerical simulations of the Mediterranean Sea outflow: Impact of the entrainment parameterization in an isopycnic coordinate ocean model. *Ocean Modelling*, **5**, 325-356.

Perot, J. B., 1993: An analysis of the fractional step method. *J. Comput. Phys.*, **108**, 51-58.

Peters, H., W.E. Johns, A.S. Bower, and D.M. Fratantoni, 2003: Mixing and entrainment in the Red Sea overflow plume. II. Turbulence characteristics. Preprint.

Price, J., and J. Yang, 1998: Marginal sea overflows for climate simulations. In *Ocean Modelling and Parameterization*, eds: E.P. Chassignet and J. Verron, pp. 155-170.

Price, J.F., and M.O. Baringer, 1994: Outflows and deep water production by marginal seas. *Prog. Oceanogr.*, **33**, 161-200.

Price, J.F., M.O. Baringer, R.G. Lueck, G.C. Johnson, I. Ambar, G. Parrilla, A. Cantos, M.A. Kennelly, and T.B. Sanford, 1993: Mediterranean outflow mixing and dynamics. *Science*, **259**, 1277-1282.

Simpson, J.E., 1987: *Gravity currents in the environment and the laboratory.* John Wiley and Sons, New York, 244 pp.

Simpson, J.E., 1982: Gravity currents in the laboratory, atmosphere, and the ocean. *Ann. Rev. Fluid Mech.*, **14**, 213-234.

Simpson, J.E., 1972: Effects of the lower boundary on the head of a gravity current. *J. Fluid Mech.*, **53**, 759-768.

Simpson, J.E., 1969: A comparison between laboratory and atmospheric density currents. *Quart. J. Roy. Met. Soc.*, **95**, 758-765.

Simpson, J.E., and R.E. Britter, 1979: The dynamics of the head of a gravity current advancing over a horizontal surface. *J. Fluid Mech.*, **94**, 477-495.

Smith, P. C., 1975: A streamtube model for bottom boundary currents in the ocean. *Deep-Sea Res.*, **22**, 853-873.

Smith, R.A., 1991: Maximization of vortex entropy as an organizing principle in intermittent, decaying, two-dimensional turbulence. *Phys. Rev.*, **A 43**, 1126-1129.

Smyth, W.D., and J.N. Moum, 2000: Length scales of turbulence in stably stratified mixing layers. *Phys. Fluids*, **12**, 1327-1342.

Thorpe, S.A., 1977: Turbulence and mixing in a Scottish loch. *Philos. Trans. Roy. Soc. London*, **A286**, 125-181.

Tseng, Y., and J.H. Ferziger, 2001: Mixing and available potential energy in stratifed flows. *Phys. Fluids*, **13**, 1281-1293.

Tufo, H. M., and P. F. Fischer, 1999: Terascale Spectral Element Algorithms and Implementations. Gordon Bell Prize submission, *Proc. of the ACM/IEEE SC99 Conf. on High Performance Networking and Computing*. IEEE Computer Soc., CDROM.

Tufo, H. M., P. F. Fischer, M. E. Papka, and K. Blom, 1999: Numerical simulation and immersive visualization of hairpin vortices. presented at Supercomputing '99, Portland, OR, preprint ANL/MCS-P779-0899, Argonne National Laboratory.

Turner, J.S., 1986: Turbulent entrainment: the development of the entrainment assumption, and its applications to geophysical flows. *J. Fluid Mech.*, **173**, 431-471.

Webster, C.A.G., 1964: An experimental study of turbulence in a density stratifed shear flow. *J. Fluid Mech.*, **19**, 221-245.

Willebrand, J., B. Barnier, C. Böning, C. Dieterich, P. Harrmann, P.D. Killworth, C. LeProvost, Y. Jia, J.-M. Molines, and A.L. New, 2001: Circulation characteristics in three eddy-permitting models of the North Atlantic. *Prog. Oceanogr.*, **48**, 123-161.

Winters, K.B., P.N. Lombard, J.J. Riley, and E. A. D'Asaro, 1995: Available potential energy and mixing in density-stratified fluids. *J. Fluid Mech.*, **289**, 115-128.

Winton, M., R. Hallberg, and A. Gnanadesikan, 1998: Simulation of density-driven frictional downslope flow in z-coordinate ocean models. *J. Phys. Oceanogr.*, **28**, 2163-2174.

Wood, I.R., 1965: Studies of unsteady self preserving turbulent flows. *Univ. of N. S. W., Aust. Water Res. Lab. Rep.*, no. 81.

Domain size $(L_x, L_z = H, L_y)$	in 2D: $(10^4\,m\,,10^3\,m)$; and in 3D: $(10^4\,m\,,10^3\,m\,,2\times10^3\,m)$
Slope angle	$\theta = 3.5°$
Rayleigh number	$Ra = 5\times10^6$
Prandtl number	$Pr = 1$
Diffusivity ratio	$r = 2\times10^{-2}$
Viscosities	$\nu_h = 1.17\,m^2s^{-1}$ and $\nu_v = 2.34\times10^{-2}\,m^2s^{-1}$
Diffusivities	$K_h = 1.17\,m^2s^{-1}$ and $K_v = 2.34\times10^{-2}\,m^2s^{-1}$
Salinity range	$\Delta S = 1.0\,psu$
Number of elements (x, z, y)	in 2D: $(50\,,8)$; and in 3D: $(50\,,8\,,10)$
Polynomial degree	$N = 10$
Number of grid points	in 2D: 4×10^4, and in 3D: 4×10^6
Time step	$\Delta t = 0.85\,s$

Table 1: Parameters of the numerical simulations.

(a)

Dirichlet

free–slip wall Neumann

z=0

z=−1

x=0

periodic

symmetry

θ=3.5

no–slip wall Neumann

y=2

x=10 y=0

(b)

z=0

z=−0.2

U^{in}_{max}

z=−0.4

x=0

x=1.0
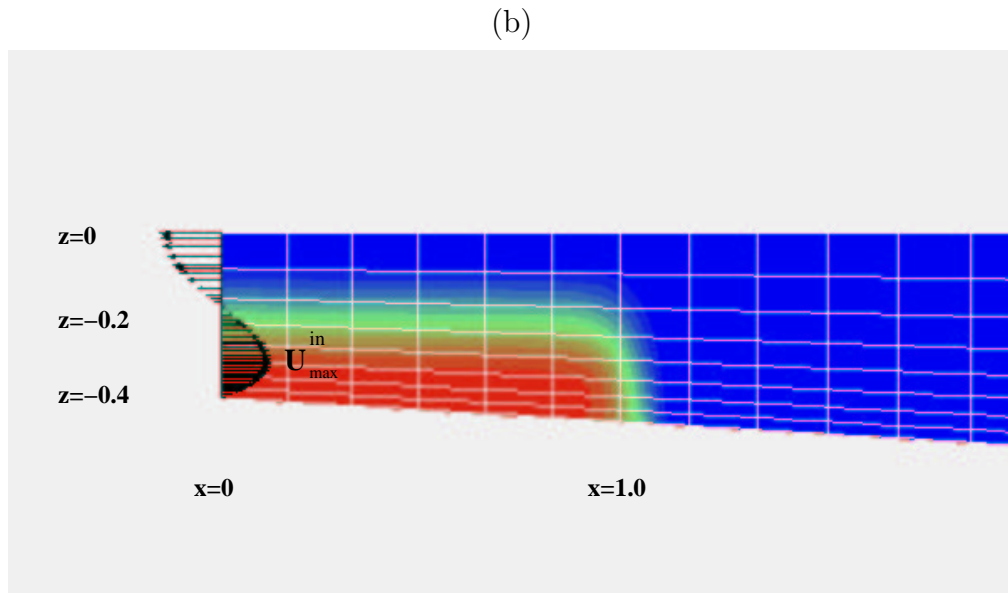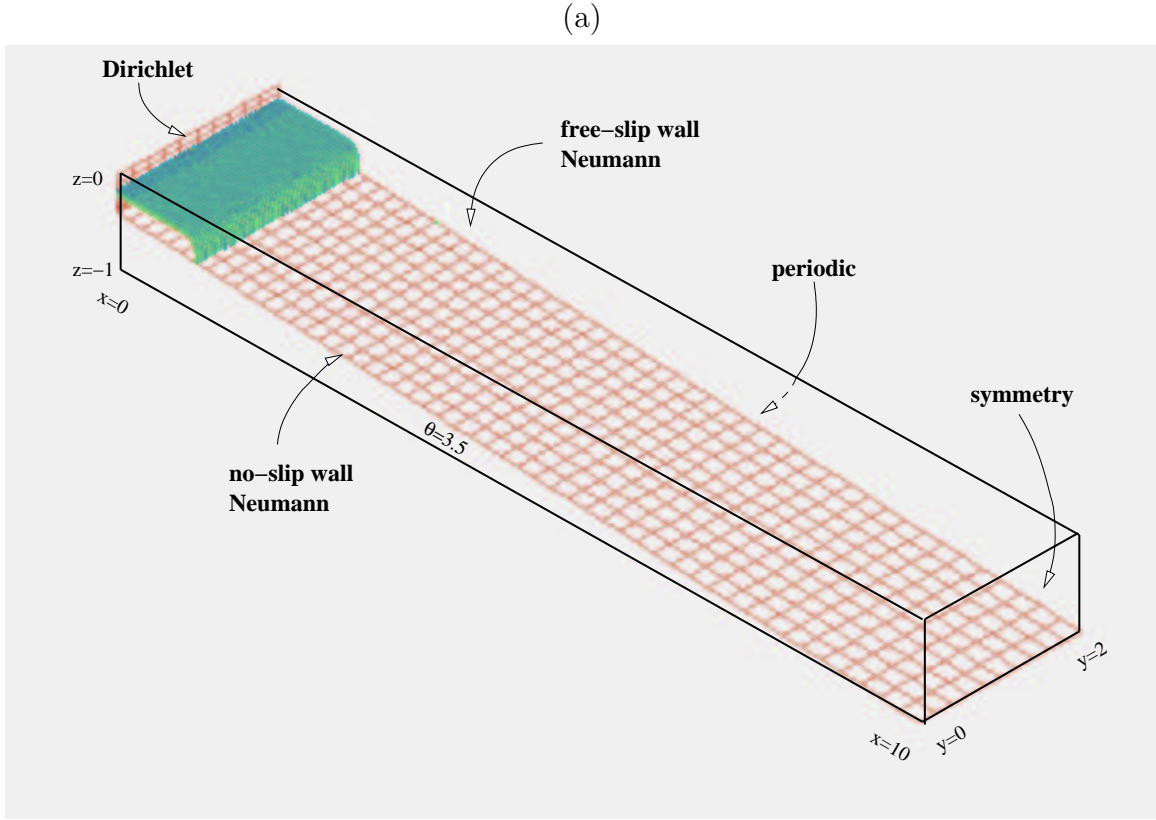
Figure 1: (a) Schematic depiction of the domain geometry and boundary conditions (length scale is in km). (b) Velocity profile at the forcing boundary and the initial distribution of salinity. Distribution of elements is depicted in the background.

(a) $t = 0$

(b) $t = 2125\,s$

(c) $t = 4675\,s$
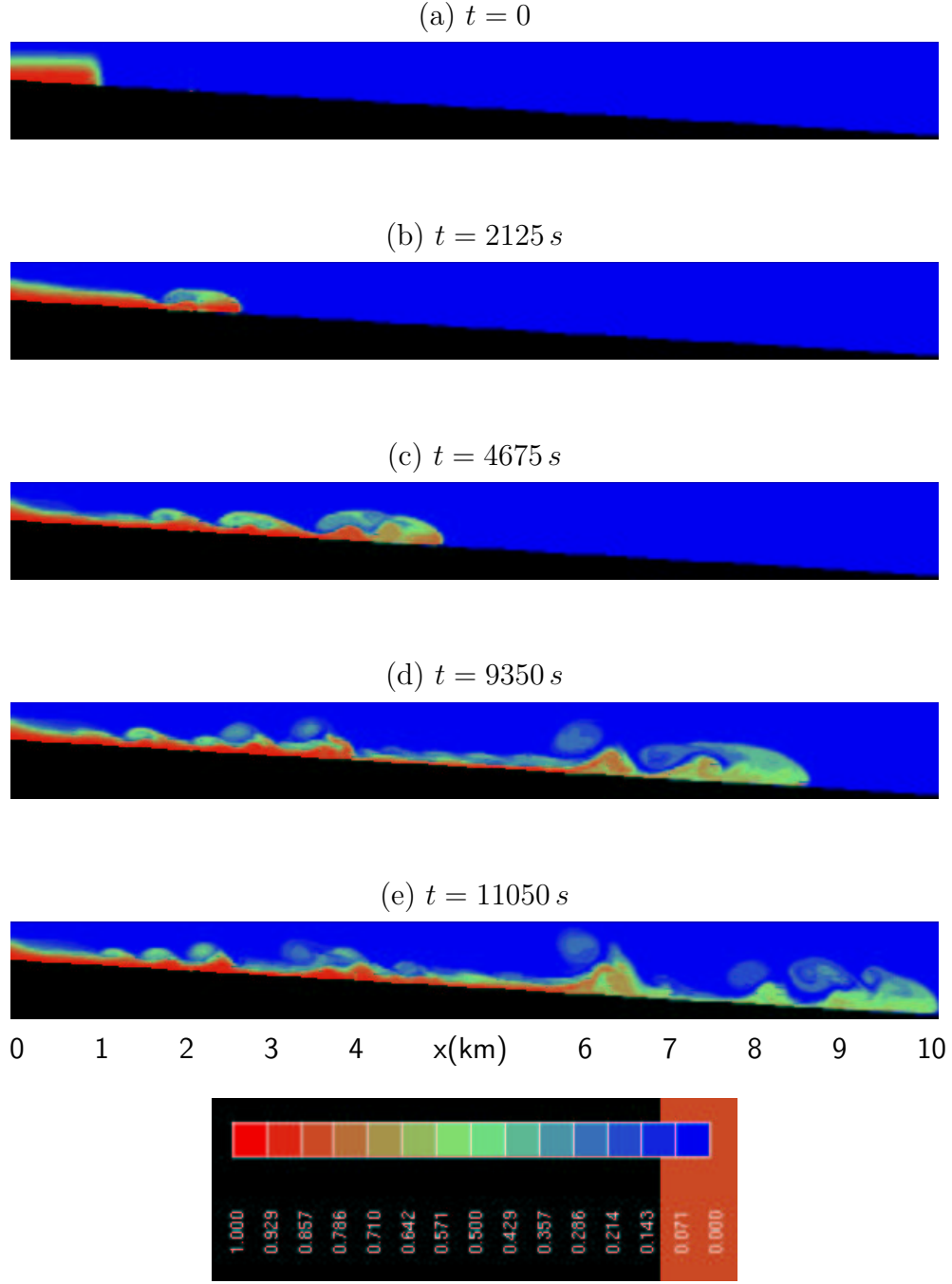
(d) $t = 9350\,s$

(e) $t = 11050\,s$

Figure 2: Salinity distribution in **EXP-2D** at (a) $t = 0$, (b) $t = 2125\,s$ ($\approx 0.6\,h$), (c) $t = 4675\,s$ ($\approx 1.3\,h$), (d) $t = 9350\,s$ ($\approx 2.6\,h$), (e) $t = 11050\,s$ ($\approx 3.1\,h$).
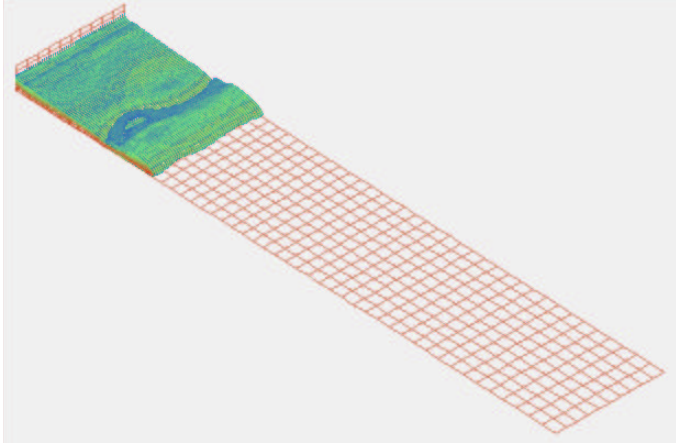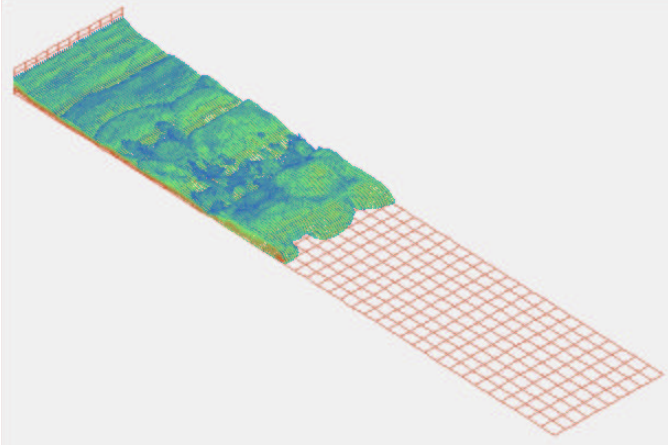
Figure 3: Distribution of salinity surface $0.3 \leq S \leq 0.6$ in EXP-3Da at (a) $t = 0$, (b) $t = 2125\,s\ (\approx 0.6\,h)$, (c) $t = 4675\,s\ (\approx 1.3\,h)$, (d) $t = 9350\,s\ (\approx 2.6\,h)$.

(a) Streamwise salinity slices at $t = 4675\,s$
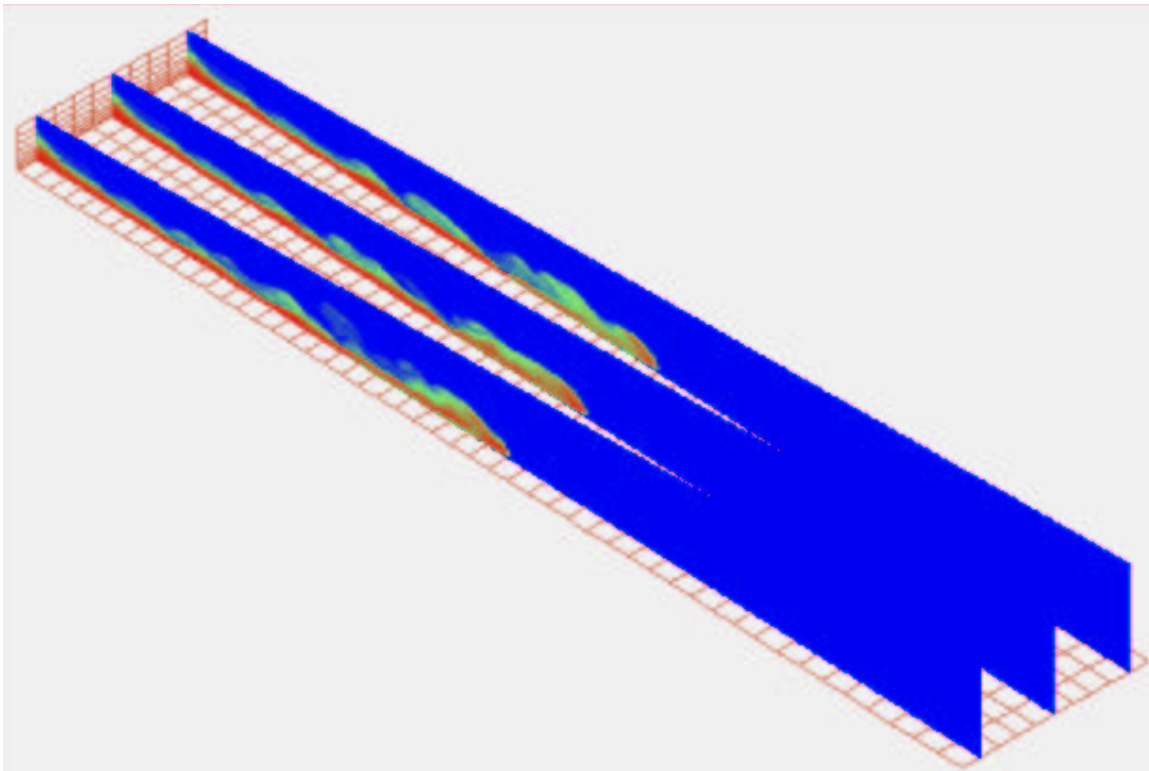
(b) Spanwise-averaged salinity at $t = 4675\,s$
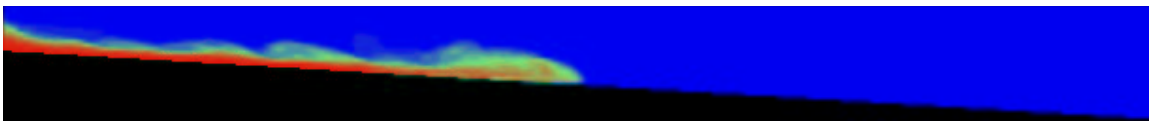
Figure 4: (a) Streamwise slices, and (b) spanwise-average of salinity distribution in EXP-3Da at $t = 4675\,s$.

(a) $t = 0$
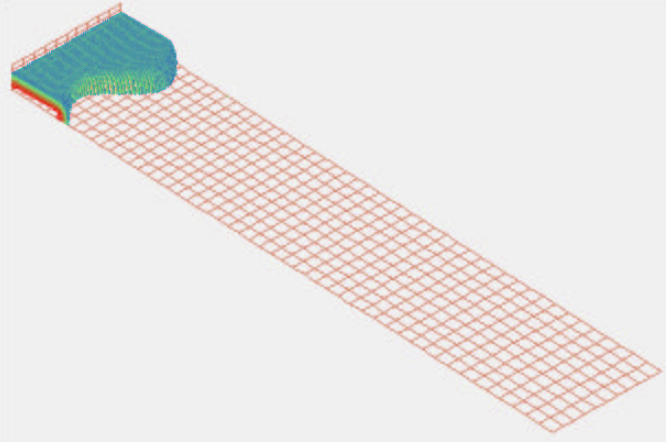
(b) $t = 2125\,s$
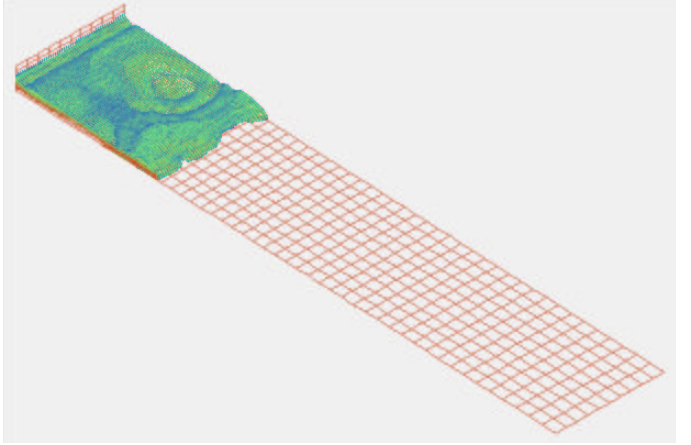
(c) $t = 4675$
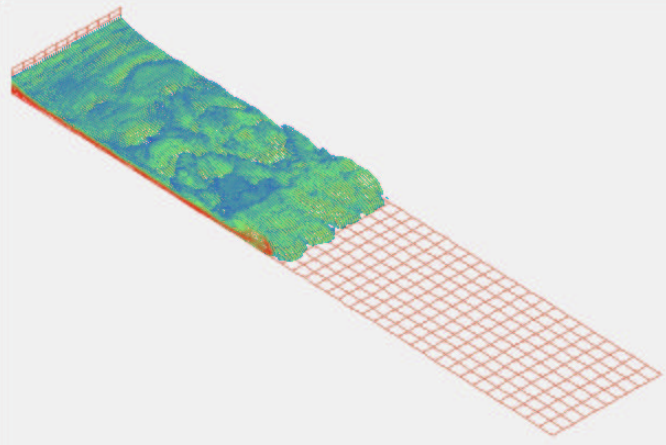
(d) $t = 9350\,s$
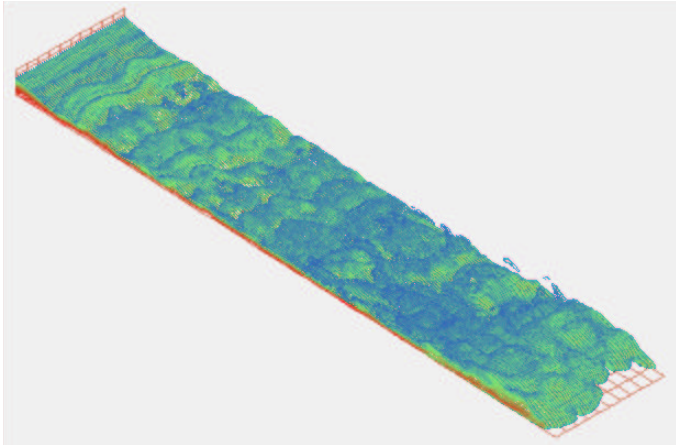
Figure 5: Distribution of salinity surface $0.3 \leq S \leq 0.6$ in EXP-3Db at (a) $t = 0$, (b) $t = 2125\,s\ (\approx 0.6\,h)$, (c) $t = 4675\,s\ (\approx 1.3\,h)$, (d) $t = 9350\,s\ (\approx 2.6\,h)$.
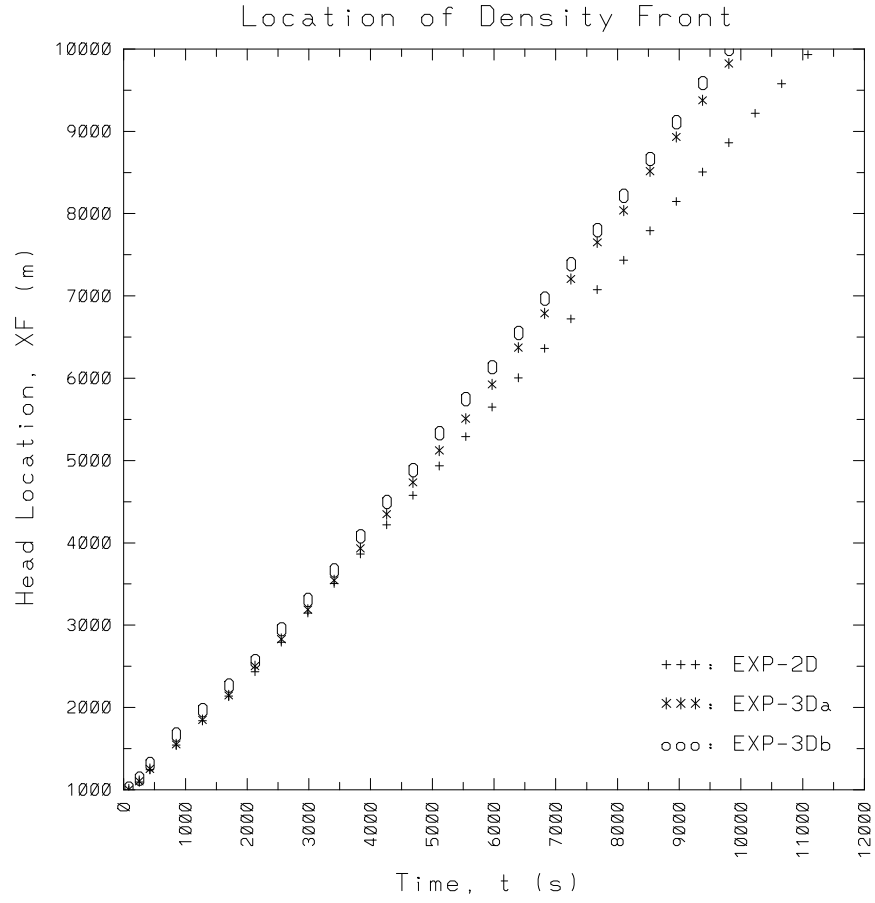
Figure 6: Position of the density front, X_F (in m) as a function of time (in s) in all experiments. Line with "+++" denotes result from EXP-2D, and lines with "***" and "ooo" denote those from EXP-3Da and EXP-3Db, respectively.
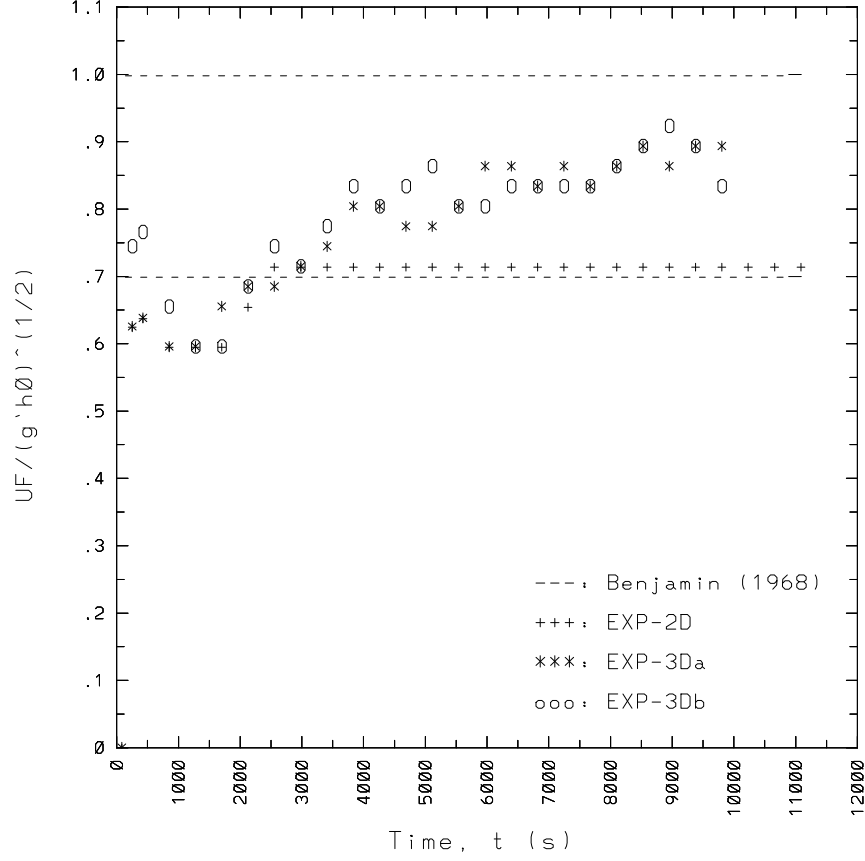
Figure 7: Descent speed normalized by the speed of internal wave for lock-exchange flows, $U_F/\sqrt{g'h_0}$. Line with "$+++$" denotes result from EXP-2D, and lines with "$***$" and "ooo" denote those from EXP-3Da and EXP-3Db, respectively. Dashed lines show theoretical results by Benjamin (1968), who found that $U_F/\sqrt{g'h_0} = 1/\sqrt{2}$ when the ratio of dense water and total water depth is 0.5, and $U_F/\sqrt{g'h_0} = 1$ when the depth ratio is 0.2.
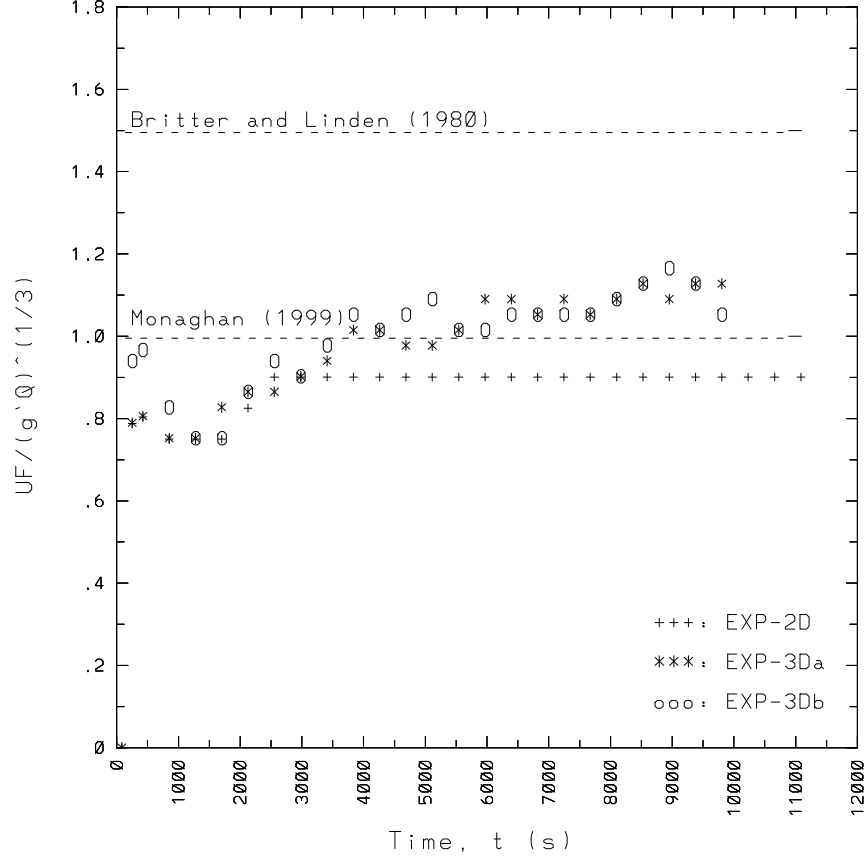
Figure 8: Descent speed normalized by the speed of input buoyancy flux, $U_F/(g'Q)^{1/3}$. Line with "+++" denotes result from EXP-2D, and lines with "***" and "ooo" denote those from EXP-3Da and EXP-3Db, respectively. Dashed lines mark the mean values from laboratory experiments by Britter and Linden (1980) $U_F/(g'Q)^{1/3} = 1.5\pm0.2$, and Monaghan et al. (1999) $U_F/(g'Q)^{1/3} = 1.0 \pm 0.1$.
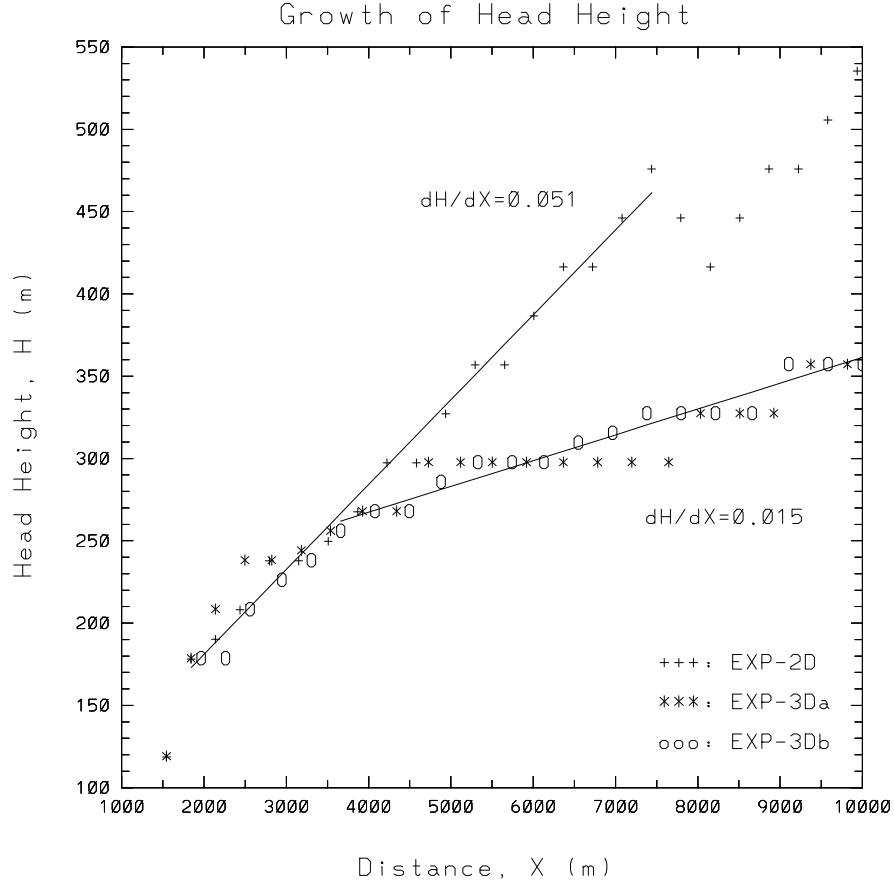
Figure 9: Change of head height $\mathcal{H}$ (in m) with distance X (in m). Line with "+++" denotes result from EXP-2D, and lines with "***" and "ooo" denote those from EXP-3Da and EXP-3Db, respectively. Solid lines show least square approximations to data points, $d\mathcal{H}/dX \approx 0.051$ for 2D phase and $d\mathcal{H}/dX \approx 0.015$ for 3D phase.
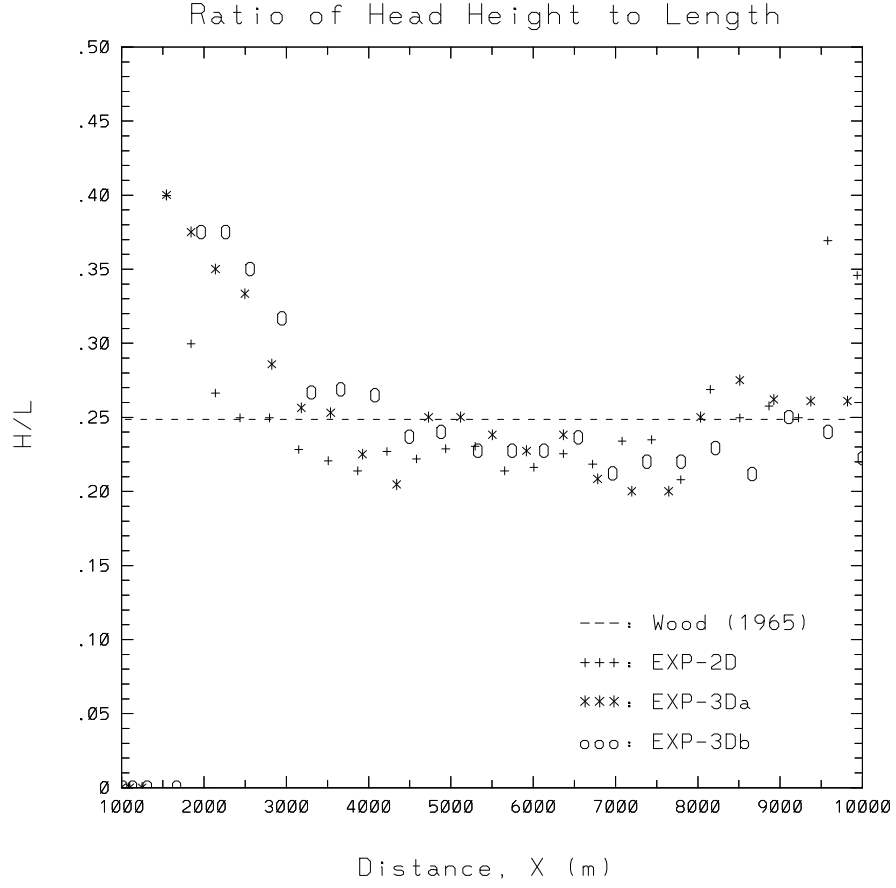
Figure 10: The ratio of head height to head length $\mathcal{H}/L$ as a function of distance X (in m). The dashed line indicated the laboratory result by Wood (1965, extracted from Fig. 9 of Britter and Linden, 1980) that $\mathcal{H}/L \approx 0.25$ for gravity current over a slope of $\theta = 5°$.
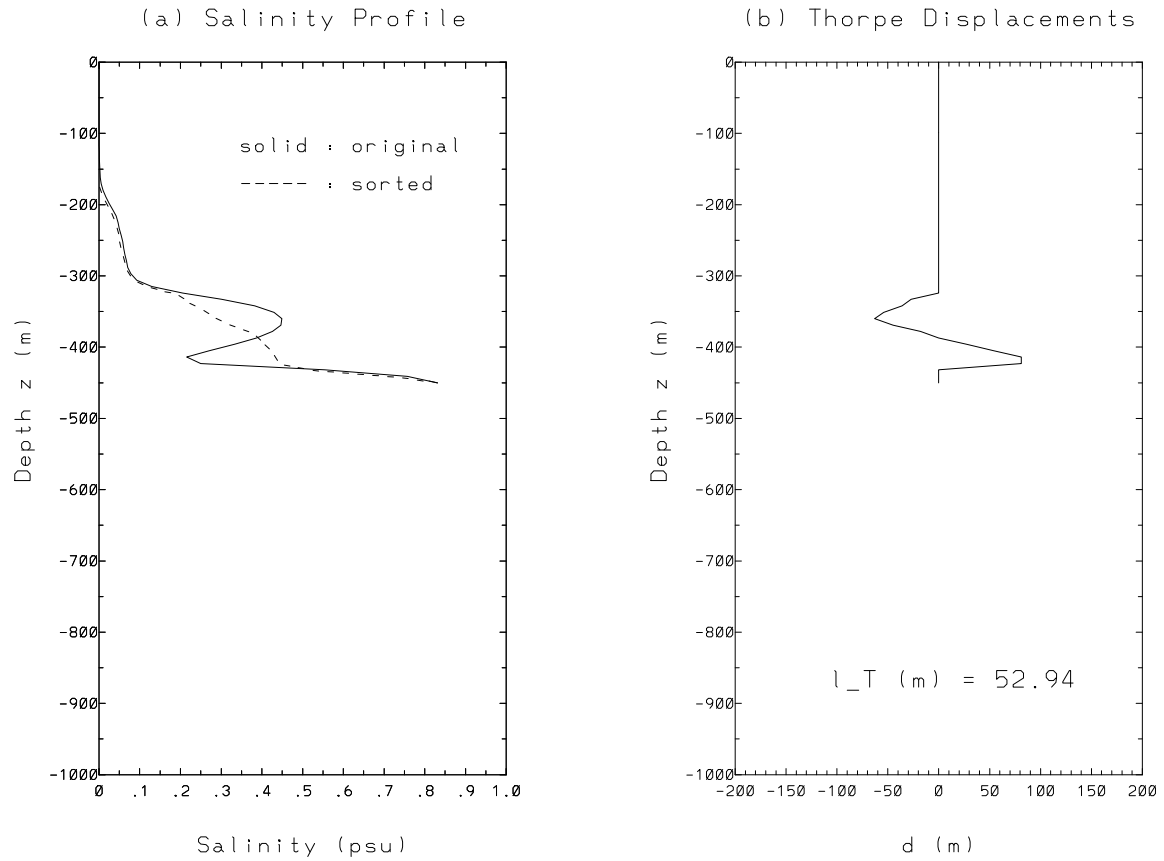
Figure 11: (a) Sample salinity profile taken from **EXP-2D** at $x = 1.5\,km$ and $t = 9829\,s$ (solid line). The dashed line shows the same values after being reordered into a stable monotonic profile. (b) Thorpe displacement, d, indicates the distance that water parcels in the original salinity profile must travel in order to reach stable stratification. Thorpe scale, $\ell_T \equiv < d^2 >_z^{1/2}$ is proportional to the scale of vertical overturning.
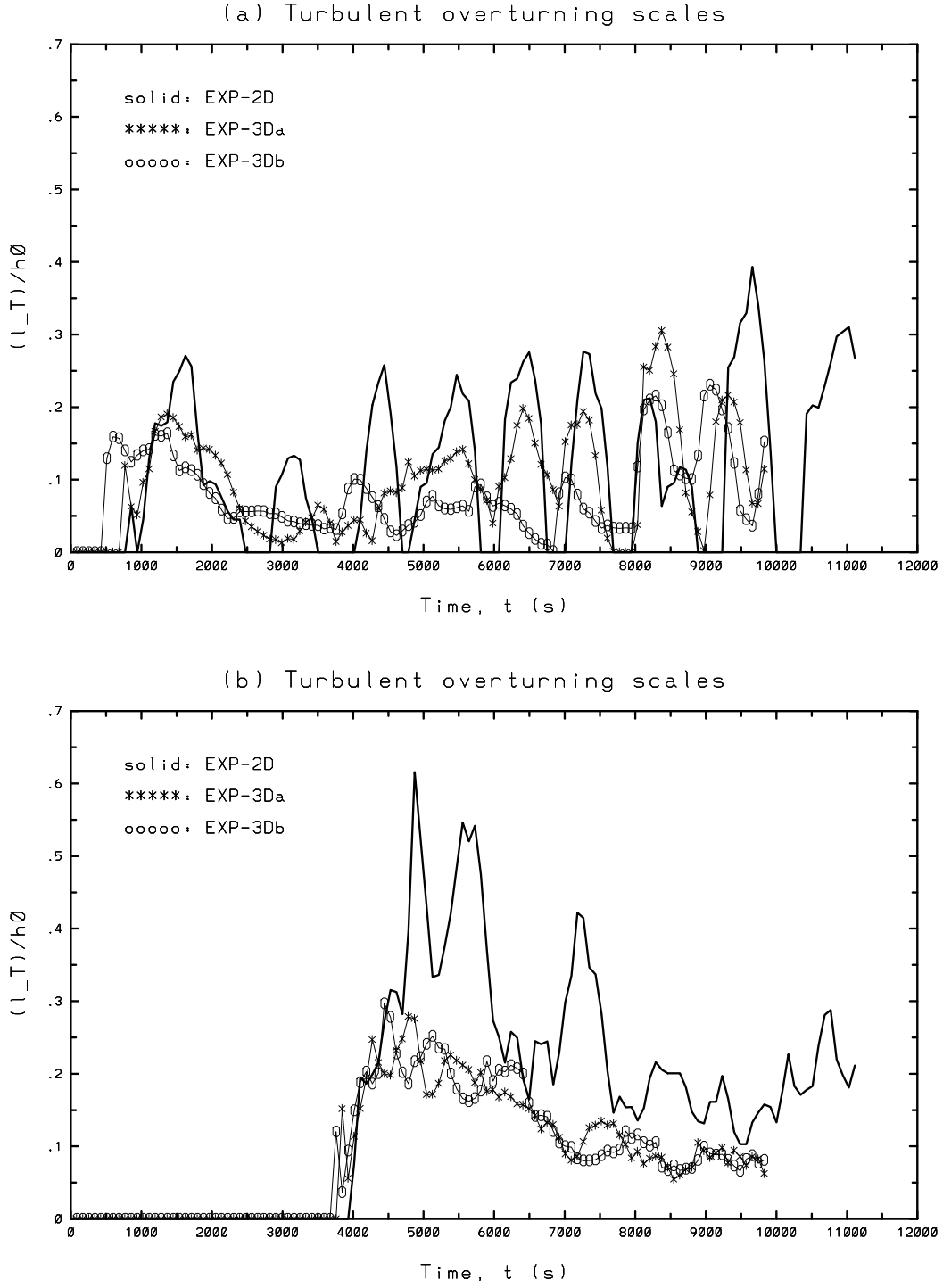
Figure 12: Average turbulent overturning scales normalized by the initial thickness of dense water column, $(\overline{\ell_T}/h_0)$, which are sampled as a function of time at (a) $x = 1.5\,km$ and (b) at $x = 4.0\,km$ in **EXP-2D** (solid lines), **EXP-3Da** (lines with "***") and **EXP-3Db** (lines with "ooo"). Defining a buoyancy time scale $t_b \equiv \sqrt{h_0/g'} \approx 169\,s$, the time axis, $t = 12000\,s$ scales to $t/t_b = 71$.
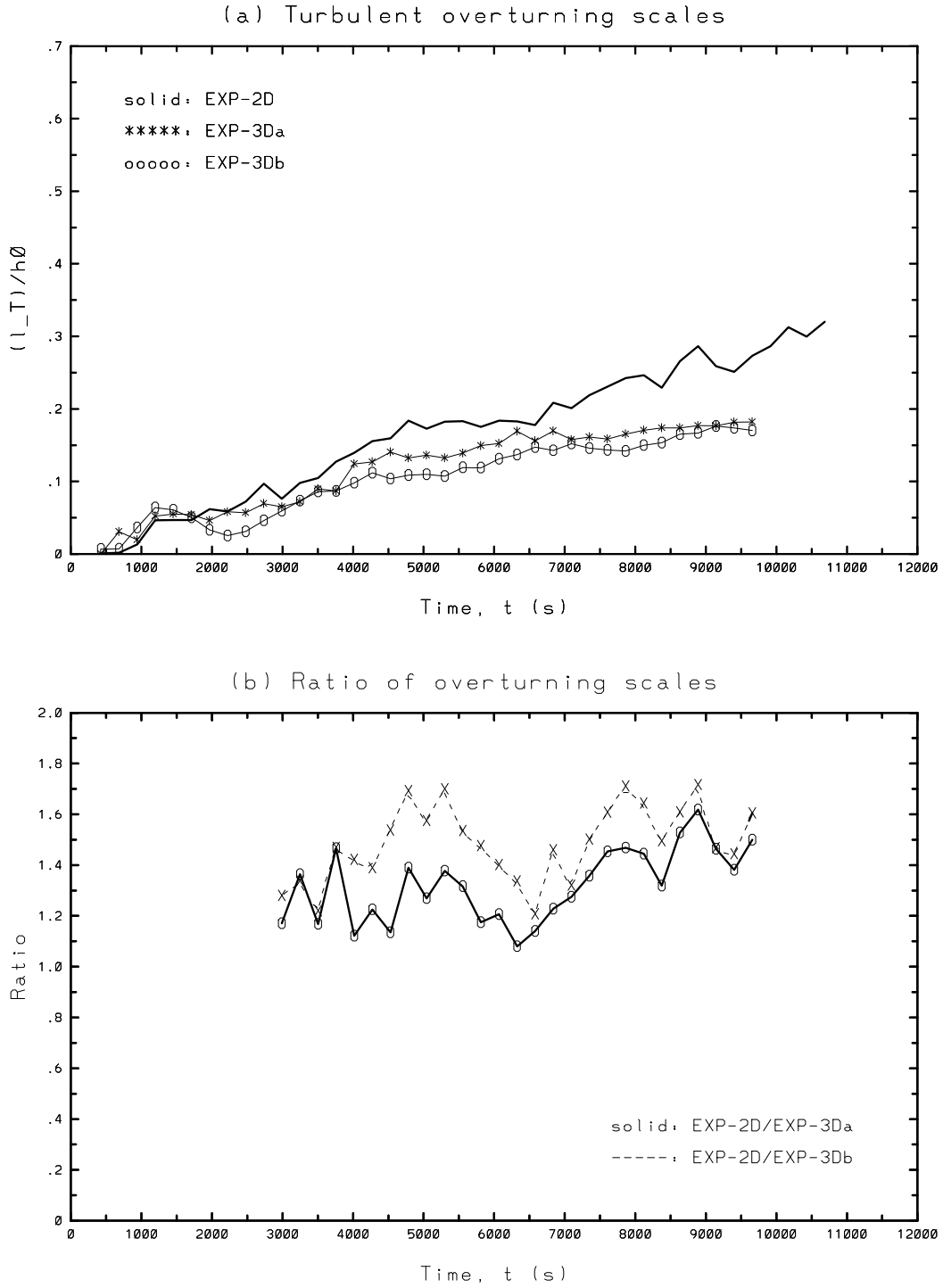
Figure 13: (a) Turbulent overturning scales normalized by the initial thickness of dense water column, $(\overline{\ell_T}/h_0)$, which are averaged over the entire length of descending plumes in EXP-2D (solid lines), EXP-3Da (lines with "***") and EXP-3Db (lines with "ooo"). (b) The ratio of 2D and 3D overturning scales, EXP-2D/EXP-3Da (solid line) and EXP-2D/EXP-3Db (dashed line).
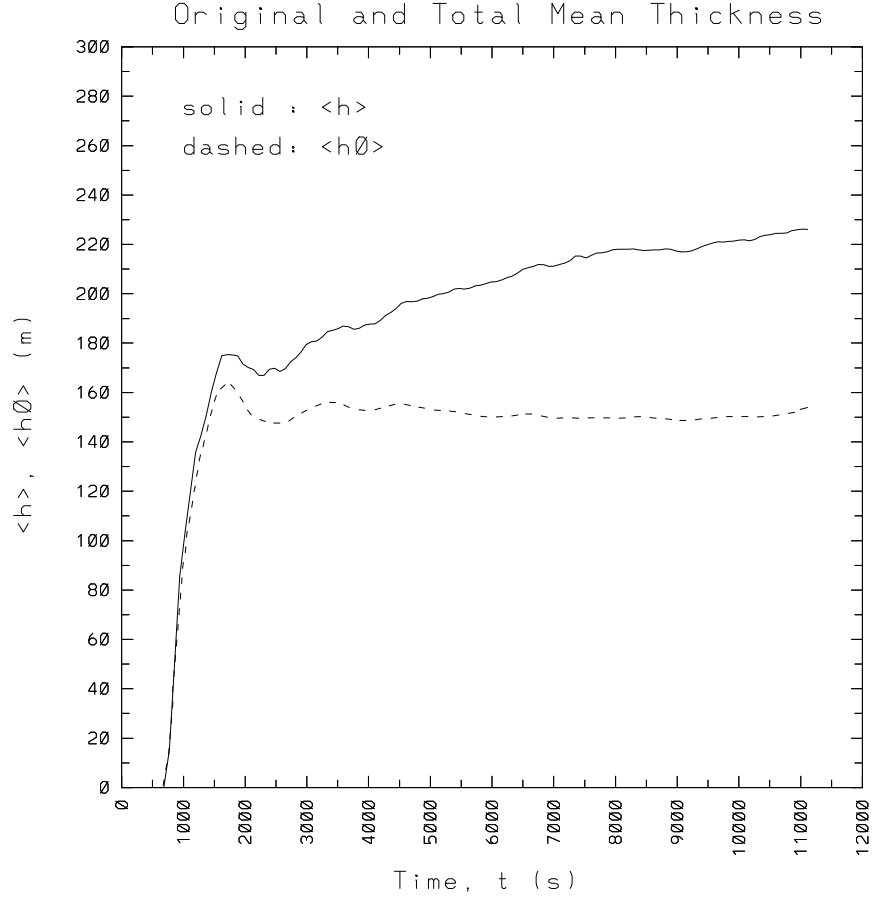
Figure 14: Time evolution of original mean overflow thickness $\overline{h_0}(t)$, and total mean overflow thickness $\overline{h}(t)$ in EXP-2D. Note that $\overline{h_0} \approx \overline{h}$ until the initial formation of the head during $1500\,s \le t \le 2500\,s$, and then $\overline{h_0}$ stabilizes around a mean value of $150\,m$, whereas $\overline{h}$ shows a steady increase due to entrainment.
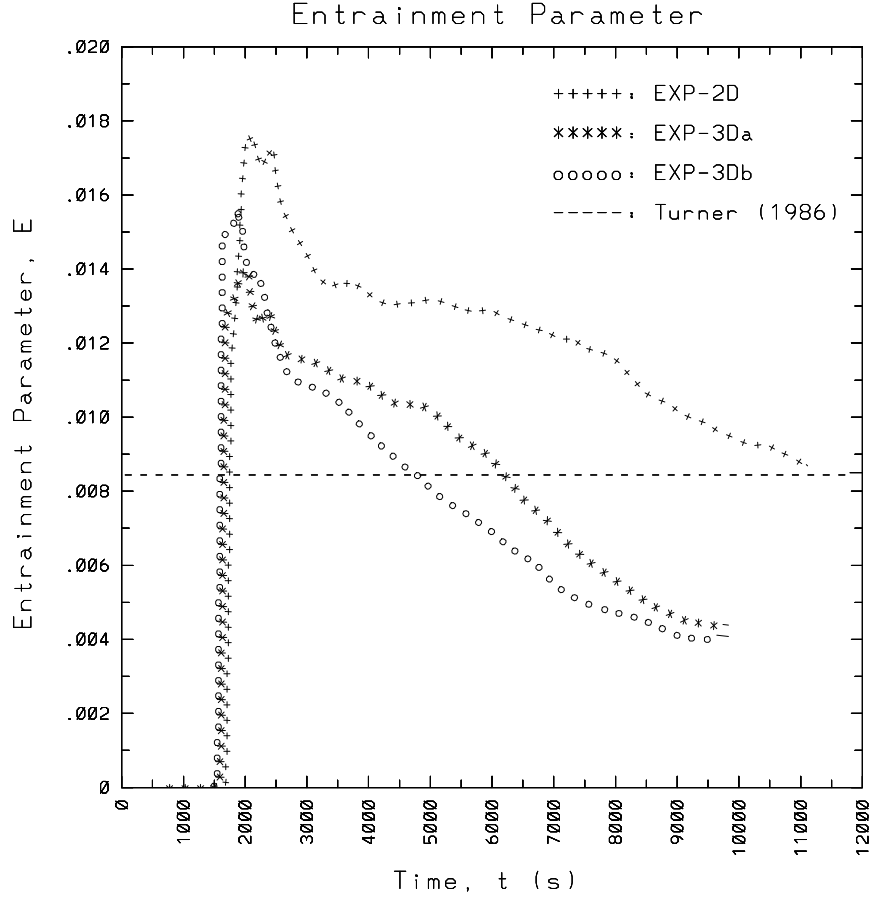
Figure 15: Time evolution of entrainment parameters $E(t)$ in all experiments. Line with "+++" denotes result from **EXP-2D**, and lines with "***" and "ooo" denote those from **EXP-3Da** and **EXP-3Db**, respectively. Dashed line marks the estimate $E = (5+\theta) \times 10^{-3} = 0.0085$ given by Turner (1986) based on laboratory experiments of Ellison and Turner (1959).